THE EXTREME ULTRAVIOLET IMAGER INVESTIGATION FOR THE IMAGE MISSION

B. R. SANDEL[1], A. L. BROADFOOT[1], C. C. CURTIS[1], R. A. KING[1], T. C. STONE[1], R. H. HILL[2], J. CHEN[2], O. H. W. SIEGMUND[3], R. RAFFANTI[3], DAVID D. ALLRED[4], R. STEVEN TURLEY[4] and D.L. GALLAGHER[5]

[1]*Lunar and Planetary Laboratory, University of Arizona, Tucson, AZ 85721, U.S.A.*
[2]*Baja Technology LLC, 1040 E. Fourth St., Tucson, AZ 85721-0077, U.S.A.*
[3]*Siegmund Scientific, Walnut Creek, CA 94595, U.S.A.*
[4]*Department of Physics and Astronomy, Brigham Young University, Provo, UT 84602, U.S.A.*
[5]*Space Science Department, NASA Marshall Space Flight Center, Huntsville, AL 35812, U.S.A.*

(Received May 25, 1999)

Abstract. The Extreme Ultraviolet Imager (EUV) of the IMAGE Mission will study the distribution of He^+ in Earth's plasmasphere by detecting its resonantly-scattered emission at 30.4 nm. It will record the structure and dynamics of the cold plasma in Earth's plasmasphere on a global scale. The 30.4-nm feature is relatively easy to measure because it is the brightest ion emission from the plasmasphere, it is spectrally isolated, and the background at that wavelength is negligible. Measurements are easy to interpret because the plasmaspheric He^+ emission is optically thin, so its brightness is directly proportional to the He^+ column abundance. Effective imaging of the plasmaspheric He^+ requires global 'snapshots' in which the high apogee and the wide field of view of EUV provide in a single exposure a map of the entire plasmasphere. EUV consists of three identical sensor heads, each having a field of view 30° in diameter. These sensors are tilted relative to one another to cover a fan-shaped field of 84° × 30°, which is swept across the plasmasphere by the spin of the satellite. EUV's spatial resolution is 0.6° or ∼ 0.1 R_E in the equatorial plane seen from apogee. The sensitivity is 1.9 count s^{-1} Rayleigh^{-1}, sufficient to map the position of the plasmapause with a time resolution of 10 min.

1. Introduction

The Extreme Ultraviolet Imager (EUV) is designed to study the distribution of cold plasma in Earth's plasmasphere by imaging the distribution of the He^+ ion through its emission at 30.4 nm. The He^+ 30.4 nm emission is the natural choice for remote sensing of the plasmasphere. Apart from H^+, which has no optical emission, He^+ is the most abundant ion in the plasmasphere. Typical peak densities are around 1000 cm^{-3}, and the He^+ ion constitutes roughly 20% of the plasma population. The He^+ outside Earth's shadow resonantly scatters the solar 30.4 nm radiation, so that the plasmasphere glows. Because the plasmaspheric He^+ emission is optically thin, the integrated column density of He^+ along the line of sight through the plasmasphere is directly proportional to the intensity of the emission. Therefore measurements are relatively easy to interpret; there is no need to consider the complication of radiative transfer effects. The He^+ 30.4-nm feature is easy

Space Science Reviews **91:** 197–242, 2000.

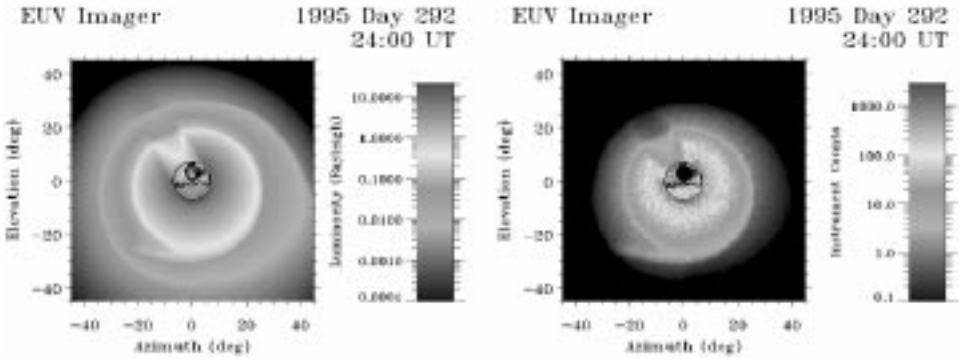

Figure 1. Left: Brightness of the 30.4-nm emission from the plasmasphere, as seen from the IMAGE apogee distance above the north pole, computed from a realistic model of He^+ distribution. The notch to the upper left of center is Earth's shadow. *Right:* Expected signal from EUV in a 10-min exposure, including realistic noise count rates and variations of sensitivity over the field of view.

to measure because it is the brightest ion emission from the plasmasphere, it is spectrally isolated, and the background is negligible.

Imaging the plasmasphere is the ideal means of monitoring changes in plasma density and distribution. IMAGE will be the first mission to provide full-plasmasphere images from outside the plasmasphere. However, a number of observations of plasmaspheric He^+ using photometers in low Earth orbit have proven the general technique of remote sensing the plasmasphere by this means (Meier and Weller, 1974, and references therein; Chakrabarti et al., 1982; Meier et al., 1998). The power of global imaging of the plasmasphere has been recognized for some years (Williams, 1990; Sandel et al., 1993). Figure 1 shows a model of the brightness distribution that we expect to see and the EUV's response. This figure emphasizes the idea that true global imaging requires a wide field of view.

2. Scientific Goals and Measurement Requirements

The plasmasphere is a central element of all processes occurring in the inner magnetosphere. For example, it influences the transport of energy from the ring current into the inner magnetosphere and reflects the small and large scale patterns of convective electric fields. The importance of the plasmasphere to inner magnetospheric processes and the inadequate state of our understanding of the plasmasphere has been detailed in recent work by Carpenter et al. (1993), Carpenter (1995), Fok et al. (1995), and Khazanov and Liemohn (1995). Many questions remain to be answered. How and where do ring current interactions through collisions, wave-particle processes, and locally induced electric fields erode the plasmasphere during the onset of storms and substorms? What is the resulting plasmaspheric influence on ring current losses? Small scale density structures of thermal plasma are formed inside and outside the plasmapause boundaries. Where do these struc-

tures form in the course of plasmaspheric erosion? Are injected ring current ions influential in the loss of thermal plasma inside the plasmapause formed by storm-time erosion? What is the fate of eroded thermal plasma as it is convected toward the dayside magnetopause? To what extent is this plasma lost and entrained within the magnetosphere? How does refilling occur and where? Can the two-stage refilling paradigm (Thomsen et al., 1998) postulated for the trough, be seen in refilling plasmaspheric flux tubes?

These are some of the questions to be addressed by the IMAGE Mission. EUV will directly address questions related to the spatial structures and their temporal evolution through observed variations in the distribution of He^+ in the inner magnetosphere. The Radio Plasma Imager (RPI) on the IMAGE spacecraft will also provide measurements of thermal plasmas. Derived densities, from those locations returning radio sounding echos, will be combined with EUV line-of-sight images to infer quantitative, global distributions of plasmaspheric plasma. Image inversion techniques will follow those to be used with energetic neutral atom images (see the papers by Perez and by Roelof in this issue). EUV images of the plasmasphere will also be combined with images of the ring current. The IMAGE Medium Energy (MENA) and High Energy (HENA) Neutral Atom imagers will observe line-of-sight integrated, global images of the ring current, over a spectrum of energies. Dynamic changes in the spatial and energy distribution of ring current ions will be compared to the corresponding state and changes in plasmaspheric plasma. The importance and morphology of ring current collisional losses with the plasmasphere and the pattern of ring current generated regional electric fields will be revealed. Wherever thermal plasma can be followed by EUV through the inner magnetosphere, it will be possible to directly infer regional and global convective electric fields. Comparing these fields with the current state of magnetospheric electric field modeling will test and advance our understanding of coupling among the solar wind, magnetosphere, and ionosphere.

To achieve these goals, EUV must:

1. accommodate a maximum 30.4-nm brightness of 10 R in the plasmasphere as well as the much brighter, localized ionospheric source,
2. measure emissions of 0.1 to 0.3 R in an integration time of 10 min,
3. have a wide field of view to encompass the entire plasmasphere in a single 'snapshot,' and
4. reject bright contaminating emissions, such as H Ly-α from the geocorona and interplanetary medium and the He 58.4-nm line emission from the ionosphere.

The instrument that we describe here provides all these capabilities.

3. Instrument Design

Effective imaging of the plasmaspheric H^+ 30.4 nm emission requires global 'snapshots' in which the high apogee of the IMAGE mission and the wide field of view

TABLE I
Principal EUV design parameters

Property	Value
Mass	15.5 kg
Power	9.0 W
Size	49.7(h) × 23.3(w) × 49.5(d) cm
Field of view	84° × 360°
Optical design	Prime focus, $f/0.8$
	Spherical mirror and focal surface
Angular resolution	0.6°
Spatial resolution*	630 km
Time resolution	10 min
Sensitivity	1.9 count s^{-1} per R

*In the equatorial plane, seen from apogee.

of the Extreme Ultraviolet Imager provide, in a single exposure, a map of the entire plasmasphere from the outside. EUV consists of three identical sensor heads serviced by common electronics and three high-voltage power supplies contained in a single unit. Each sensor head has a 30° conical field of view, and the three sensor heads are tilted relative to one another by 27° to cover a fan-shaped instantaneous field of view of 84° × 30°. As the satellite spins, the fan sweeps an 84° × 360° swath across the sky. Table I summarizes the main features of EUV.

Figures 2 and 3 show the EUV. The sensor heads are mounted between two support brackets. One of these incorporates the EUV Controller electronics and the detector electronics packages. The other mounts the high-voltage power supply. The brackets extend forward of the sensor heads to provide light baffling, and a light baffle covers the space between the brackets.

Each sensor head has its own detector electronics package, which includes preamplifiers and position-finding circuitry (Figure 4; Section 3.4). Positions of individual photoevents are transferred to the EUV Controller, which includes a microprocessor, a RAM buffer and program space, ROM, A/D converters for housekeeping information, and the required I/O capability. The Controller accepts commands from the Central Instrument Data Processor (CIDP) to select operating modes. The CIDP provides a spin-phase sync signal to the EUV, including markers for spin phase relative to the nadir and to the Sun.

3.1. SENSOR HEADS

Figure 2 illustrates the design of the sensor heads, and their characteristics are summarized in Table II. The entrance aperture consists of four segments that collectively form a nearly-complete annulus. In each of the four segments of the

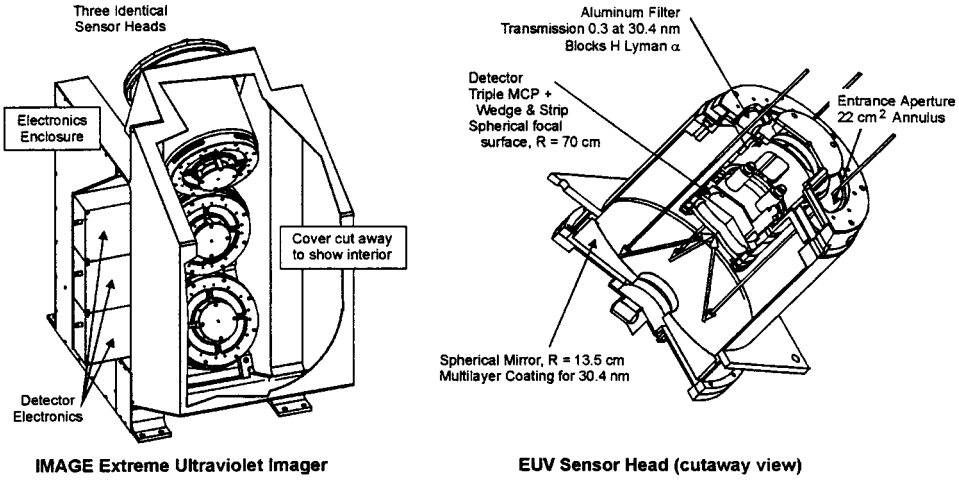

Figure 2. Left: left-front view of the EUV, with a portion of the main light baffle cut away to show the location of the sensor heads. The high-voltage power supply is mounted on the far side, hidden in this view. *Right:* cutaway drawing of a sensor head. Detector signal and bias cables are not shown here.

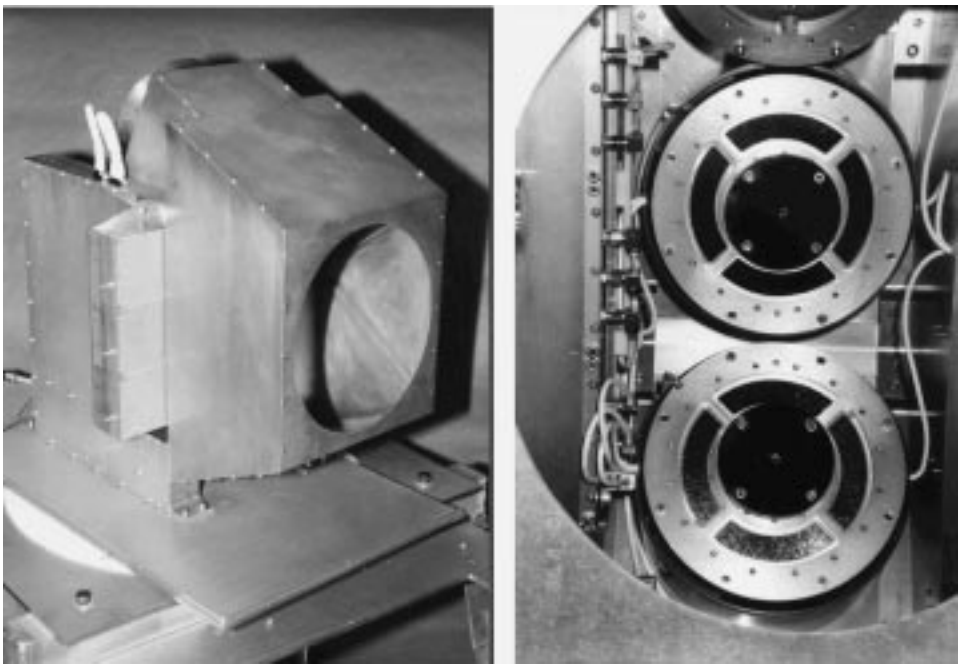

Figure 3. Left: left-front view of EUV. The main entrance aperture is the large oval opening at the right. *Right:* Looking in the main entrance aperture. The entrance apertures to two of the three sensor heads are visible.

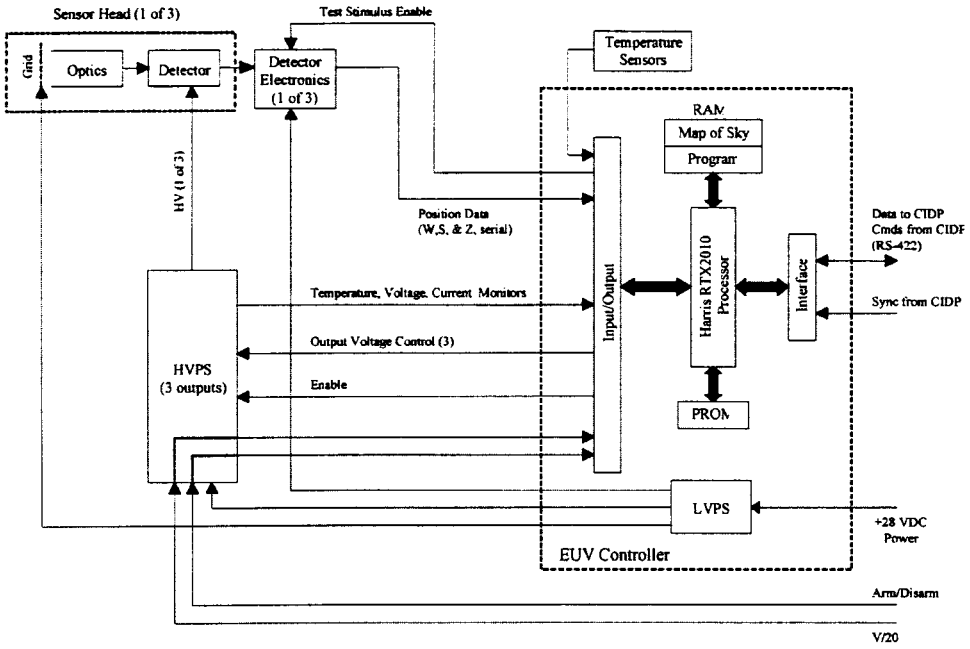

Figure 4. A simplified functional block diagram of EUV.

TABLE II
Sensor head design parameters

Property	Value
Aperture area	21.8 cm^2
Aperture diameter (outer)	8.2 cm
Aperture diameter (inner)	6.0 cm
Mirror diameter	12.3 cm
Mirror radius of curvature	13.5 cm
Focal ratio	$f/0.8$
Detector active diameter	4.0 cm
Radius of curvature of focal surface	7.0 cm

annulus is a filter (Section 3.3) that transmits the He^+ 30.4 nm line, while excluding the bright geocoronal H Ly-α line at 121.6 nm as well as other emissions. Light that passes through the filter reaches the mirror. For good reflectivity at the target wavelength, the mirror has a multilayer coating (Section 3.2) formed of uranium and silicon. Light reflected from the mirror is focused on the spherical focal surface of the sensor (Section 3.4).

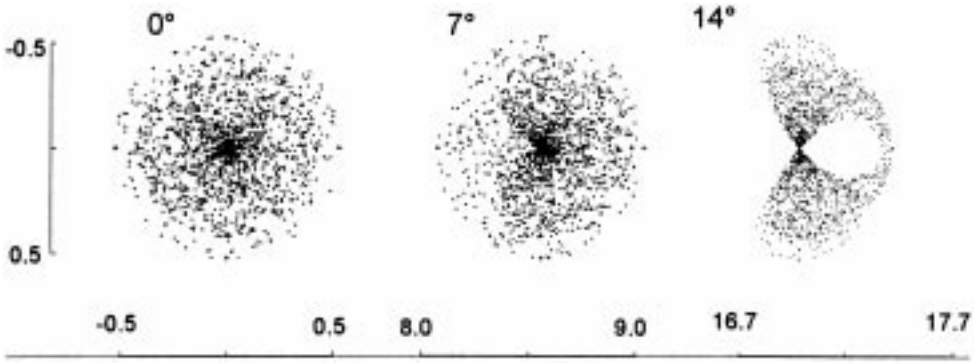

Figure 5. Spot diagrams for three field positions. The angles refer to position off-axis. The coordinates refer to position on the focal surface in mm.

We have chosen this optical design to achieve the optimum compromise of throughput, spatial resolution, and uniformity of resolution over the field. The design is similar to that used in the ALEXIS x-ray telescopes (Bloch et al., 1990) which also required a wide field of view and high throughput. In connection with the ALEXIS mission, the optical design has been analyzed in some detail (Bloch et al., 1990). Our ray-tracing studies show that angular resolution of 0.6° is to be expected, and that it will be nearly uniform over the field of view.

Figure 5 shows spot diagrams for three field positions. The on-axis spot diagram has radial symmetry, as we expect from the cylindrical symmetry of the design. At 7° off-axis, vignetting by the detector has begun, and near the edge of the field at 14° off-axis, vignetting by the detector is pronounced. The rms radius for each of the field positions is $\sim$ 0.27 mm, or $\sim$ 0.22° using the plate scale of 0.81° mm^{-1} inferred from Figure 5. For all three field positions, 50% of all rays are enclosed by a circle of diameter 0.50 mm (0.41°) and 80% of all rays are enclosed by a circle of diameter 0.72 mm (0.58°). Another measure of spatial resolution is the modulation transfer function (MTF). For all three field positions, an MTF of 50% corresponds to a spatial frequency of 1 line-pair/0.81°.

The most important effect of vignetting is to reduce the throughput at the edge of the field (Figure 6). Throughput at the nominal edge of the field, 15° off-axis, is $\sim$ 53% of its value at the center of the field. Effective throughput at the top and bottom edges of the field is also reduced by the spin-scanning, which exposes each pixel for a time proportional to the length of the chord across the field of view. To partially offset these effects, we have overlapped the fields of view of the three sensor heads by 3°. We discuss these considerations in more detail in Section 5.3.

The annular entrance aperture offers the benefit of limiting the range of incidence angles of rays at the multi-layer mirror. The multilayer must be optimized for a particular angle of incidence, and it has reduced reflectivity at other incidence angles. Figure 7 shows the distribution of incidence angles of rays that pass through the entrance aperture and reach the detector. In spite of the large (30°) field, essen-

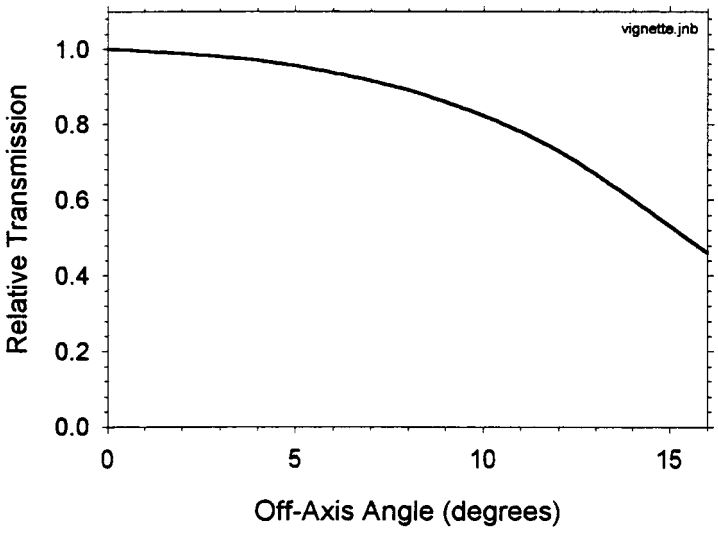

Figure 6. Vignetting by the detector reduces the effective throughput at the edge of the field.

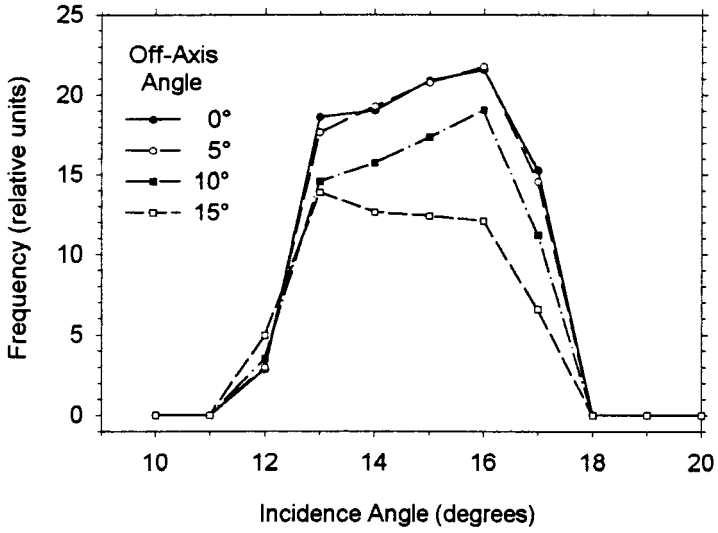

Figure 7. Rays that will eventually reach the detector fall in a limited range of angles of incidence on the mirror.

tially all of the useful rays have incidence angles in the range 12°–18°. This is within the range of incidence angles over which the multi-layer coating achieves satisfactory reflectivity (Section 3.2.3).

With our sensor head design and the expected signal levels, we can tolerate a few tiny holes in the filters. Holes may develop owing to environmental stress and other factors (Vallerga et al., 1992). The principal effect of a small hole in the filter is to admit the unwanted H Ly-α line from the geocorona. Radiation at this

wavelength from an extended source such as the geocorona that enters the sensor head will illuminate the detector roughly uniformly, thereby reducing the signal-to-noise ratio for the target wavelength. We have two lines of defense against H Ly-α: (1) the filters themselves, and (2) the response of the detector. Regarding the latter, we have chosen to use the microchannel plates bare, omitting a deposited photocathode material. A deposited photocathode would increase the response at 30.4 nm; however, practical candidate materials would increase the response to H Ly-α by a larger factor than at 30.4 nm. For perfectly hole-free filters, maximum response (and SNR) would be achieved with the highest possible quantum efficiency at the target wavelength. However, if we admit the possibility that the filters may develop some holes, then we can have a better SNR by using the bare microchannel plate. For worst-case conditions including a 30.4 nm signal level of 0.1 R, a geocoronal background of 10^4 R, and an integration time of 10 min, the crossover falls at an open area of 4×10^{-4} cm^2, nearly the same size as one of the 'panes' in the mesh that supports the filter material.

The front of the sensor head is insulated from the main body and held at +15 V to exclude low-energy ions from the sensor head. The sensor heads are copiously vented to avoid damage to the filters owing to the acoustic environment at launch. All of the vent openings are covered by a fine mesh that is also held at +15 V.

3.2. MULTILAYER MIRRORS

In this section we discuss the design, fabrication and testing of the mirror coatings. Relatively high, though relatively narrow band, normal-incidence reflection ($>$ 65%) has been achieved for wavelengths between about 11.0 nm and 14.4 nm (90 to 110 eV) (Skulina, 1995 and references cited therein). Achieving high reflectance at near-normal incidence for other wavelengths has been more difficult. The challenges for fabrication include:

1. Almost all materials are highly absorbing in the extreme ultraviolet. This means that only a few interfaces in a multilayer will contribute to its reflectance.
2. Surface contamination and corrosion are particular problems since first-row elements, especially carbon through oxygen, have remarkably high absorptance over the 25 to 120 nm range. As little as 0.05 nm of an oil film or surface oxide can significantly change a mirror's reflectance.
3. The mirrors are highly curved (f/0.8).
4. The H Ly-α 121.6 nm and He I 58.4 nm lines (10 and 21 eV) are much brighter than the 30.4 nm (41 eV) line. While the 121.6 nm line is blocked by an Al filter, Al is relatively transparent to 58.4 nm radiation. There is no acceptable filter for blocking 58.4 nm that meets the other mission requirements.
5. The mirrors' optical response must be retained over a 6° range of incidence angles (12°–18° from normal), which is relatively broad for multilayer mirrors.

We have designed and fabricated a new kind of extreme ultraviolet mirror that retains high 30.4 nm reflectivity with low 58.4 nm reflectivity. We discuss the

design of these mirrors in Section 3.2.1, their fabrication in Section 3.2.2, and their testing in Section 3.2.3.

3.2.1. *Multilayer Design*

The design requirements called for a mirror that had a high ($> 20\%$) reflectivity at 30.4 nm (He^+ $1s \rightarrow 2p$) and low ($< 0.2\%$) reflectivity at 58.4 nm (He $1s^2 \rightarrow 1s2p$), both measured at $14.5° \pm 3.5°$ to the surface normal. These specifications are challenging because most materials have much higher single layer reflectivities at 58.4 nm than at 30.4 nm. For example, the normal incidence reflectance of molybdenum at 58.4 nm is 24%.

To reflect well at 30.4 nm and poorly at 58.4 nm, the top part of the stack which reflects well at 30.4 nm must act as an antireflection layer at 58.4 nm. Such mirrors with dual optical function in the extreme ultraviolet have not previously been designed or built.

Because of the procedures established for the installation of these mirrors and their likely future environments we also decided that the mirrors must be optically stable in dry air for at least three weeks.

3.2.1.1. *Initial Design.* We developed and used a variety of computational tools to model reflectance of multilayers composed of many possible material combinations. These included incorporation of the genetic algorithm (GA) (Lunt and Turley, 1999a; Lunt, 1999) to optimize material selection and layer thicknesses for best performance.

The optimizer permitted design of fully aperiodic multilayer coatings. The additional degrees of freedom over a periodic design permitted us to design mirrors with better predicted performance, especially in achieving low 58.4 nm reflectance. We chose the genetic algorithm for this design because it allowed optimization with discrete variables (the choice of materials), provided a search for a global minimum, and was simple to constrain. Details about the genetic algorithm and these design efforts can be found in Lunt and Turley (1999b, 1998).

Uranium, which had been identified early as a leading candidate for 30.4 nm, also proved to be the only metallic material for the high index (the so-called absorber) layer which was also suitable for producing a multilayer for low 58.4 nm reflectance. The highest predicted reflectivity using the genetic algorithm was for an aperiodic Y_2O_3/Al mirror.

In the end, we did not use the aperiodic design in our final fabrication. The changing thicknesses of the aperiodic stacks from layer to layer made it difficult to characterize them using X-ray diffraction (see Section 3.2.2). Without these growth diagnostics, we found it too difficult to optimize the stacks empirically during growth. Fabricating a Y_2O_3/Al stack presented the additional complication of requiring RF rather than magnetron DC sputtering because Y_2O_3 is an insulator. The GA, on the other hand, called our attention to the possibility of using oxidized

uranium as the top layer material and showed us the proper range of thicknesses to consider.

3.2.1.2. *Final Design.* From top to bottom the flight mirror coating consisted of:

1. A thin layer of UO_x produced by oxidation of 1.5 nm of uranium within a few minutes of exposure to air. If the film oxidizes to UO_3 the layer will swell to over three times its original thickness. This oxide functions as the top high index layer in the multilayer when considering high reflectance at 30.4 nm. This is the first time this has been done for XUV multilayers. The oxide is also largely responsible for the low reflectance at 58.4 nm.
2. Six and one- half periods of bilayers with 12.8 ± 0.01 nm of silicon and 5.3 ± 0.1 nm of uranium.
3. One 10.6 nm layer of uranium, twice the uranium thickness used in the other layers. This extra-thick bottom layer allows the coating to be released from the glass if recoating is necessary, without compromising optical performance.

Our final design also differed from the optimized initial designs because the latter designs did not account for factors which significantly changed the reflectivities. These factors included:

- The models assumed the boundaries between layers were smooth and abrupt. While the roughness was probably less than 0.5 nm rms, the diffusion of Si into the U layers may have been as deep as 5–10 nm.
- The optical constants for sputtered U in this region are uncertain (Fennimore et al., 1999; Squires, 1999).
- Oxidation of the multilayers may have occurred during and after growth. Oxygen is highly absorbing in the XUV. Oxidation affects the density and thickness of the layers as well.

Experimental evidence for each of these contributions is discussed in Section 3.2.2.

3.2.2. *Multilayer Mirror Fabrication*

All films were deposited by DC magnetron sputtering. The uranium target was depleted uranium bought from Manufacturing Sciences (Oak Ridge, TN). The 4-inch diameter, heavily doped silicon target was purchased from CERAC. The sputtering was done in a chamber evacuated to a base pressure of $< 3 \times 10^{-6}$ torr with a CRYO-TORR 8 cryopump. The chamber was then backfilled to a pressure of 2.8×10^{-3} torr with ultrahigh purity (99.999% pure) argon passed through an UltraPure (NuPure Corporation) line filter which removed residual N_2, O_2, H_2O, and H_2. A plasma was generated in the argon by applying a potential (about 400 V for U and 550 V for Si) between the target and dark space shield. A magnetic field confined the plasma to the area near the target. Argon ions striking the target sputtered U or Si atoms from the surface. These accumulated on the mirror surface at a rate that was calibrated by x-ray diffraction (XRD) measurements on test samples.

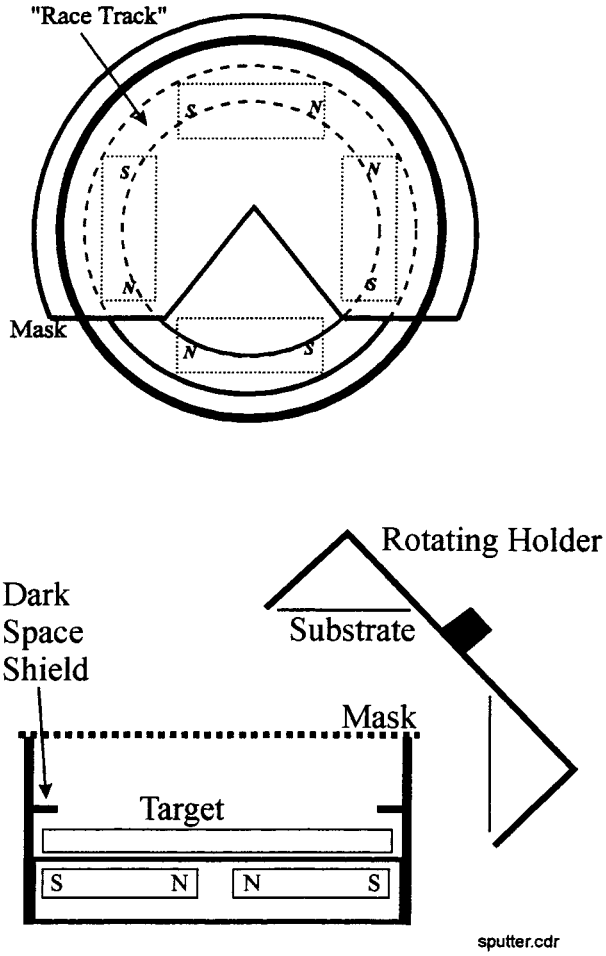

Figure 8. Schematic of the sputtering system. *Top:* top view. *Bottom:* side view, showing the mask and target used.

We achieved the required uniformity across the highly curved surface of the mirrors by rapidly rotating the mirrors in a specially constructed holder above the sputter targets and by masking the sputter target to block atoms coming from the side of the target closest to the inside of the chamber.

The mirror and holder were hung from a carousel and angled so that about half of the holder would pass above the target. At any given instant only a sector of the mirror was above the sputter source. The mirror was spun rapidly on its axis, however, so that in less than a second each part of the mirror a given distance from the center was exposed to the sputtering target for the same amount of time. Figure 8 shows schematics of the deposition system. We designed the appropriate masks by iterative deposition and XRD measurement cycles. Using these masks

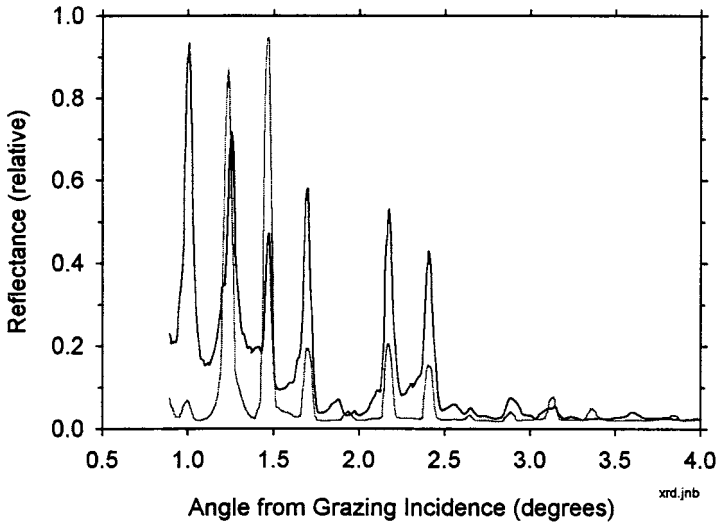

Figure 9. Reflectance of a mirror trial flat at the Cu K-α line as a function of angle measured from grazing incidence.

and carefully orienting the mirror holder, we produced coatings whose thickness varied by only about $\pm 1\%$ from inside to outside.

Under our final growth conditions, the sputtering guns were kept at a power of 78 W for Si and 80 W for U. The guns were run for 5 min to 1 hr until the voltages stabilized. The layer thickness was controlled by the time the mirror spent over each gun. From the XRD measurements, we determined the sputtering times necessary to obtain the desired thicknesses were about 360 s for silicon and about 70 s for uranium.

3.2.2.1. *Characterization.* We used small silicon wafer flats for trial depositions to prepare for coating the mirrors and as witness pieces that we coated simultaneously with the flight mirrors. These have coatings with the same thickness as the mirrors. Other flat trial samples were coated independently of the flight mirrors. The trial and witness samples were used to characterize the multilayers using XRD, atomic force microscopy (AFM), Auger electron spectroscopy (AES) depth profiling, and transmission electron microscopy (TEM).

Figure 9 shows an example of a typical XRD measurement at the Cu K-α line at 0.15406 nm. The relatively narrow peaks due to constructive interference of reflections from the various layers are evidence of a good periodic stack. From the spacing and relative heights of the peaks, we were able to determine U and Si layer thicknesses to within about 0.1 nm. As mentioned earlier, aperiodic stacks produced an irregular pattern that was difficult to interpret.

Preliminary data indicate that U/Si and U/Al stacks are very similar in surface morphology, roughness, and overall oxidation characteristics. Our data for compa-

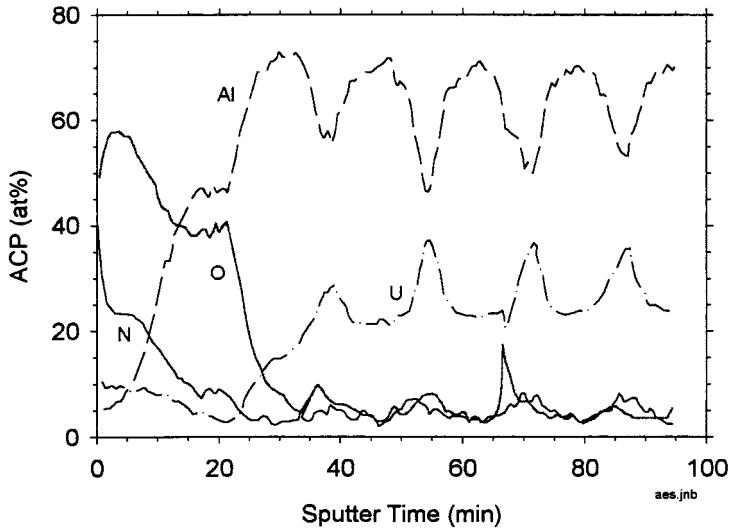

Figure 10. Depth profile measurements by Auger electron spectroscopy on trial mirror flats. The resolution of the depth shown in the figure is about 1 nm. The relative strengths of the Auger signals from different elements have not been taken into account.

rable U/Al stacks is of higher quality, so we present that here. Based on our AFM and TEM measurements on similar multilayer samples consisting of U/Al stacks, we expect the rms roughness of the layers to be about 0.5 nm.

Figure 10 shows an example of the results of AES measurements on trial U/Al samples (Fennimore et al., 1999). From these measurements we concluded that significant oxidation occurred in the top layers of the stack, and that there may be oxygen between layers in the stack. We added a UO_x cap to the production mirrors to reduce this problem.

The AES measurements of the U/Al samples also suggest the possibility of significant diffusion of Si into the U layers of the U/Si stack. Our experiments with chemically etching the coatings from the mirrors using aqua regia (a mixture of HCl and HNO_3) showed that the thickness of the bottom layer of uranium needed to be greater than 10 nm to work. This required release layer thickness provides secondary evidence that silicon diffuses into the first 5–10 nm of the underlying uranium.

Because even depleted uranium is naturally radioactive, we computed the rate of particle emission from the uranium in the mirrors and compared it to expected ambient backgrounds. Measurements were also made of the sensitivity of the MCP detector to radiation from the mirrors. Particle-induced MCP signals are comparable to the measured intrinsic dark count rates of the detectors.

3.2.3. *Multilayer Mirror Testing*

The reflectivities of the flight mirrors at 30.4 nm and 58.4 nm were measured within hours of their fabrication. The measurement system consisted of a McPherson 629 hollow cathode source filled with He and connected to a McPherson Model 225 1-m scanning monochromator. Typical operating conditions for the hollow cathode source were a base pressure of 2×10^{-6} torr, He pressure of 0.35 torr, and a current of 0.25 A. The operating pressure in the monochromator was kept below 10^{-4} torr. The monochromator used a Pt-coated grating blazed for 42.0 nm at near-normal incidence.

Using an atomic source with a monochromator gave us radiation limited only by the linewidths of the spectral lines ($\ll$0.1 nm) from the source. Our measured line widths were limited by the achievable monochromator resolution (about 0.025 nm). Since the light was incident on the monochromator and mirrors near normal incidence, we assumed it was unpolarized.

Radiation from the monochromator was detected with one of two detectors. The first was a cooled, back-thinned CCD camera from Princeton Instruments. It had a 1.25-cm square sensitive area with 512×512 pixels. The camera gave us a measure of the spatial uniformity of the beam from the monochromator and of the spatial resolution of our system. The flux from the source varied by about a factor of two over the size of the spot. A given area of illumination varied by 10% to 20% in intensity over time periods of tens of minutes. The second detector, an Amptektron MD-501 channeltron assembly, was used for quantitative measurements of intensity. Its relatively small detection area sampled a spatially uniform portion of the beam detected by the CCD camera. Typical measurements had a signal to noise ratio of several thousand.

Absolute reflectivity measurements were made on a reference mirror by measuring its signal from the channeltron detector at an equal distance from the monochromator with and without reflecting from the reference mirror. This process was repeated several times for each wavelength to enable us to compensate for any long-term drifts in the source intensity. The reflectivities of the flight mirrors were measured relative to the reference mirrors in a chamber where radiation reflected from either one could be measured within minutes of each other. The comparisons were made several times over periods of 30–60 min to enable us to account for any long term drifts in the source intensity.

Figure 11 shows the reflectivity of a typical flight mirror as a function of angle measured from the center of the mirror. The roll-offs near 7° and 25° occurred when the beam spot spilled over the edges of the mirrors. The reflectivities in the figure include a compensation for varying intensity as the mirror was rotated about its axis, which caused the spot to wander slightly on the detector.

In addition to the reflectivity measurements at BYU, we also measured the mirrors in the LPL EUV calibration facility (Section 5.1) at wavelengths of 30.4 nm and 58.4 nm. For these measurements, the reference detector was facing antiparallel to the beam, and located on the optic axis with the apex of the channeltron

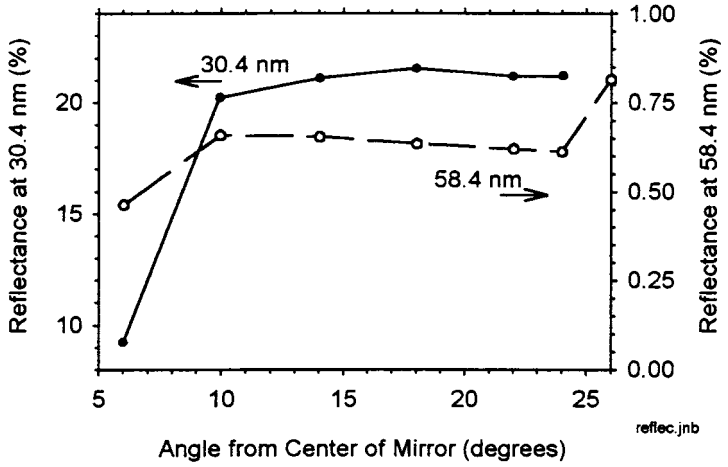

Figure 11. Reflectivity of a typical flight mirror as a function of angle measured from the center of the mirror.

cone near the focal point. The mirror and reference detector were fixed in position relative to one another and were scanned as a unit to trace a 4-mm diameter beam along two perpendicular diameters. At all points in the scan the beam remained parallel to the optical axis of the mirror, so the angle of incidence varied from 8° at the inner edge to 26° at the outer edge of the mirror. We assessed the background count rate in the reference detector by noting the response when the test beam passed through the central hole in the mirror. This background rate was about 1% for the 30.4-nm measurements and 15–20% for the 58.4-nm measurements. We cross-calibrated the reference detector against the continuous monitor between each mirror test. This required repositioning the reference detector to face into the input beam. Figure 12 shows the measured reflectivities at the two wavelengths for mirror 9, which is typical of the three flight mirrors.

Although our testing of the mirrors showed that the multilayer coatings were not particularly subject to degradation by oxidation, we protected the coatings using normal procedures for handling and storing EUV optics. We stored the mirrors in boxes purged by dry N_2, and when the mirrors had been installed in sensor heads, we kept the heads under dry N_2 purge to the extent practical. For shipping the mirrors, we designed and fabricated special containers made of anodized aluminum that were purged and then sealed for travel.

3.3. FILTERS

The filter material was chosen to provide high transmission at the target wavelength of 30.4 nm, while attenuating the unwanted H Ly-α emission from Earth's geocorona and the interplanetary medium. The filters consist of a 150-nm thick layer of aluminum supported by a nickel mesh having a wire spacing of 0.36 mm and an open area of 93%. The aluminum material was permitted to oxidize naturally

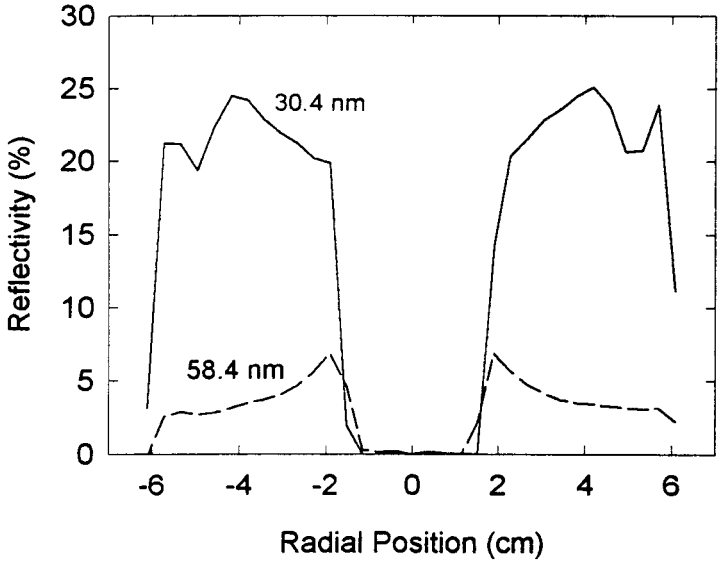

Figure 12. LPL measurements of the reflectivity of mirror 9.

on both sides. This oxide coating stabilizes the material and provides the additional benefit of reducing the transmission of the He 58.4 nm line. This emission is expected to be weak in the plasmasphere, but can be quite bright in Earth's ionosphere. A strong response to the ionospheric He 58.4-nm emission could lead to high count rates when Earth is in the field, and thus compromise measurements of 30.4-nm radiation under that condition.

We measured the transmission of the filters by mounting them in flight configuration, *i.e.* four filters were held in the circular filter support. Using a beam of diameter 4 mm, we scanned the filter fixture in a circular pattern consisting of 72 measurement points distributed uniformly over 360° and repeated at five different radii spanning the range from the inner edge to the outer edge of the filters. After each circular scan, between changes in the scan radius, we measured the unattenuated beam by translating the open center part of the filter support into the beam line.

Our measurements of the transmission of all 12 of the flight filters at 30.4 nm showed excellent uniformity from filter to filter and from position to position within each filter. The measured transmission at 30.4 nm was $33 \pm 2\%$, where the uncertainty refers to variations with sample position and between samples, and not to the measurement uncertainty. We estimate the relative uncertainty in the transmission measurement to be $\sim$1%.

To characterize the filters at the two other wavelengths of principal interest, 58.4 nm and 121.6 nm, we selected one filter from each of the four production batches of flight filters. Using the technique described in the previous paragraph, we found the transmission at 58.4 nm for the four samples to be 12%, 15%, 16%,

Figure 13. Photograph of the EUV curved surface flight MCP sensor. The active area is 4 cm in diameter, and its radius of curvature is 7 cm.

and 18%. Variations from position to position within the same filters were negligible in all four samples. At the H Ly-α wavelength, the transmission of the filters was below our measurement limit of $\sim 1\times10^{-4}$. Models show that the transmission at this wavelength is about 10^{-7}, which is well below our ability to measure using our present equipment.

3.4. DETECTOR SYSTEM

3.4.1. *Detector Design*

We have developed a novel photon counting detector scheme with a spherically curved microchannel plate (MCP) stack and wedge and strip readout for the EUV instrument (Figures 13 and 14). The system includes two main elements, the detector and the detector electronics. The detector consists of a Kovar-alumina brazed body assembly containing the MCPs and readout anode. The detector electronics consists of three boards, amplifier, ADC and interface electronics, necessary to encode photon event data. Incoming photons strike the bare surface of the MCP, where they may eject photo-electrons, which are multiplied and deposited onto a wedge and strip anode. The charge is proportionately divided among the wedge, strip and zigzag electrodes, and then the signals are transferred to the detector

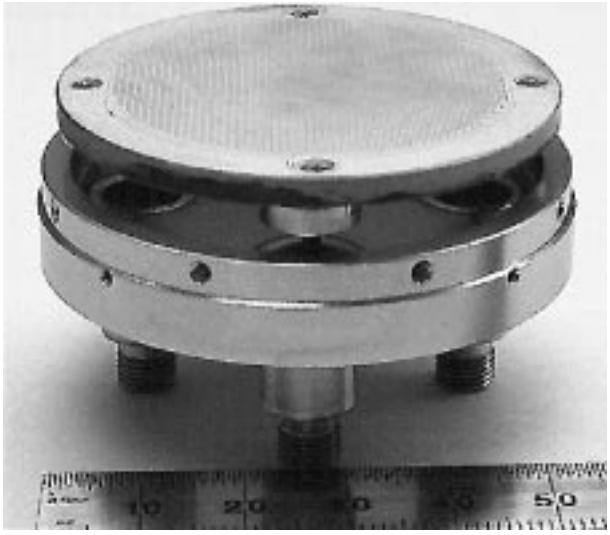

Figure 14. EUV flight detector anode subassembly showing the flat wedge and strip readout anode and flange.

electronics. Each of the three signals is amplified and converted to digital form before being sent to the EUV controller and subsequently converted to X,Y photon positions. Four flight detectors, one backup flight detector and one engineering unit have been built and tested.

The last few years have seen an increase in the use of detectors with curved-surface MCPs (Priedhorsky et al., 1998; Barstow et al., 1985; Barstow and Sansom, 1990; Siegmund, 1988) in applications that require a curved focal surface, such as Rowland circle spectrographs and fast imagers. MCP manufacturers do not routinely produce MCPs with spherically curved surfaces, so special care is necessary in the design and implementation of these devices. Techniques for curving the MCP surfaces include lapping and polishing of each MCP surface before core glass etching, and thermal slumping of the MCPs. Barstow et al. (1985) have shown this system to work well with a pair of MCPs having a small interplate gap with an interplate potential, and have subsequently applied this technique to the MCPs for the ROSAT wide field camera (Barstow and Sansom, 1990). However, the MCP curvature for EUV is considerable (7 cm radius for a 4 cm field of view). The EUV requirement is essentially the same as the highly curved MCP configurations used to match a high-speed optical system for the EUV astrophysics mission ALEXIS 1 (Priedhorsky et al., 1998. For ALEXIS the MCPs were produced by lapping and polishing pairs of MCPs having length-to-diameter (L/D) ratio = 120:1 to the required surface finish prior to etching and removing the MCP core glass. This method is expensive because it uses large amounts of MCP glass to achieve the required shape. Furthermore, the gain, gain uniformity, and quantum detection efficiency were relatively poor.

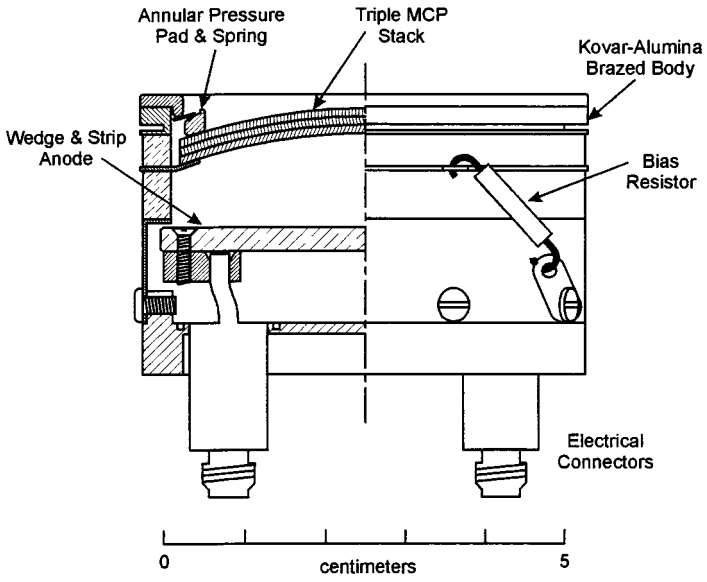

Figure 15. EUV detector design cutaway showing the individual elements of the detector.

The EUV MCP stack configuration uses three 4.6 cm diameter, 80:1 L/D MCPs with 12 μm pores, and a 7-cm radius input surface, with resistances of $\sim$ 100 MΩ per MCP. The top MCP has a 0° pore bias angle and the middle and bottom MCPs have 13° bias angles. Each MCP was thermally slumped to a spherical shape, and the MCPs were placed in direct contact as a back-to-back stack. Since the MCPs have high curvature (Figure 13), they were slumped to slightly different radii for each side of each MCP. The radii at the interface between any two MCPs were specified to ensure that the surfaces were in close contact when the MCP stack was mounted in the detector unit. The MCP stack is circumferentially clamped into the brazed body assembly using a pressure pad and annular spring arrangement (Figure 15). The pressure pad has one chord covering an area of the MCP (Figure 13) so that the in-orbit cosmic ray background can be monitored. We had considerable problems in obtaining good MCP performance in terms of gain uniformity and quantum detection efficiency. The gain varied with position as a result of the non-uniform curvature of the MCPs. A number of manufacturing techniques were explored to achieve a satisfactory curvature match. Ultimately we found one method that seems to give reasonable results. This produced broad (90%) pulse amplitude distributions with little position dependence, which is considerably better than the severe position dependencies that characterized the ALEXIS detectors.

The MCP stacks were mounted $\sim$1 cm above a wedge and strip position readout anode (Figure 14), and $\sim$300 V was applied across the MCP-to-anode gap using a resistor mounted on the external wall of the brazed body. Initially we used a spherically-curved wedge and strip anode substrate, but changed this to a flat substrate which provided better linearity performance. The anode design used is

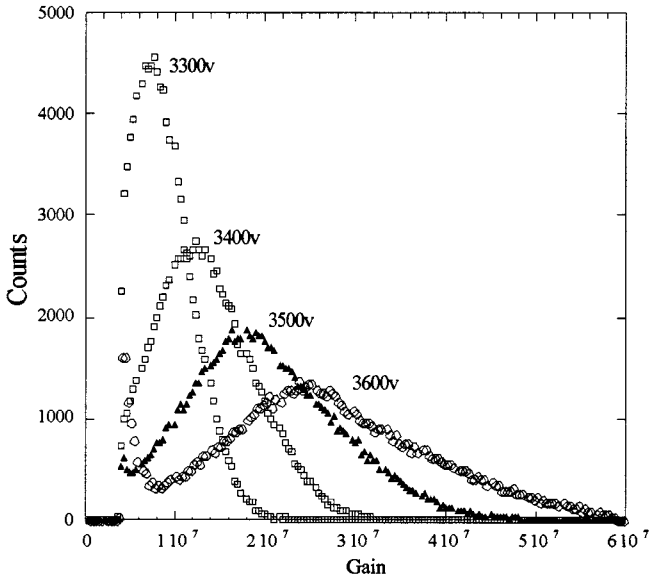

Figure 16. Pulse height distributions for the flight #05 EUV detector.

a standard three element array (Siegmund et al., 1986b) with a 0.1 cm period, covering a circular area of 4.2 cm diameter. Signals from the wedge and strip anode electrodes were connected to cables via SMA feedthroughs on the detector base (Figures 14 and 15).

3.4.2. *Performance*

3.4.2.1. *Gain and Pulse Height Characteristics.* An important indicator of the MCP stack performance is the pulse height distribution of the single photon events. The gain and pulse height distribution (PHD) measurements were accomplished with uniform 253.7 nm illumination from a pen ray lamp using a fused silica diffuser. The measured gain as a function of voltage for the #05 detector MCP set is shown in Figure 16. In general the pulse amplitude distributions of the curved surface MCPs display characteristics similar to the equivalent configuration of flat MCPs (Fraser, 1984).

The width (FWHM) of the pulse height distribution as a function of gain for all sets of curved MCPs was considerably broader than we would expect from flat MCPs, however. We can compare the fully illuminated detector PHDs to the PHD for an isolated illuminated area. The PHD for the spot illumination is narrower (60% FWHM, Figure 17) than the uniformly illuminated case (120% FWHM). This effect arises mainly from variations in gain across the highly curved MCPs. The largest contributor to the gain variations is the accuracy of fit of the MCPs onto each other in the stack. Small gaps between the MCPs will increase the electron cloud spread and thus increase the local gain. The best illustration of this can be seen in the flat field discussions where gain maps are shown. The variation

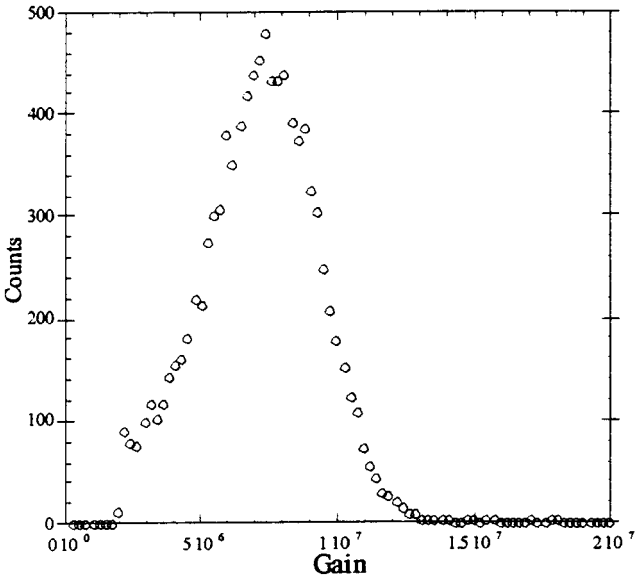

Figure 17. Pulse height distribution for a 1 cm beam at 58.4 nm, #05 EUV MCP detector.

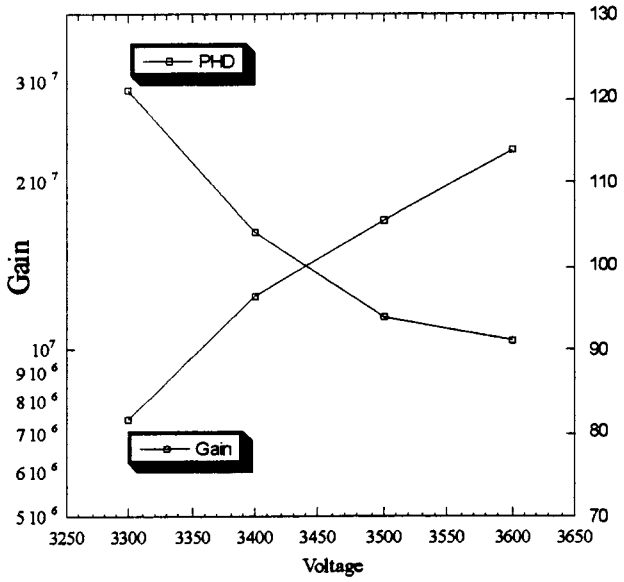

Figure 18. FWHM of the pulse height distribution and gain as a function of voltage for the flight #05 EUV MCP detector compared with COS program QDE's.

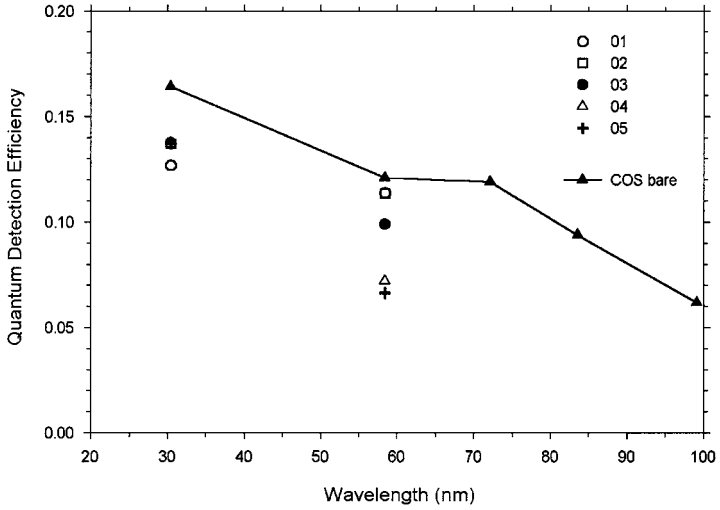

Figure 19. Quantum detection efficiencies for the flight MCP sets as a function of wavelength.

of the pulse height distribution from MCP stack to MCP stack was found to be considerable, which is indicative of the inherent variations in the spherical shapes of the MCPs.

The shape of the gain vs. voltage curves (Figure 18) for the EUV MCPs is also similar to that observed for three 80:1 L/D MCPs in a back-to-back arrangement (Siegmund et al., 1986a,b; Siegmund et al., 1985). The peak gains are about 2×10^7 with 3600 V applied across the detector. The applied voltage for a 10^7 gain varies between 3400 V and 4100 V for the different MCP stacks, due to variations in MCP stack gaps and in the secondary electron emission coefficient.

3.4.2.2. *Quantum Efficiency.* The quantum detection efficiency (QDE) of the detectors was measured at 30.4 nm and/or 58.4 nm to give a measure of the quality of the UV response. Each MCP stack was calibrated against a NIST standard windowless UV diode at an input angle of about 20° to the MCP centerline. The results show a significant variation of the efficiency (Figure 19). For comparison, a measurement of some nominal QDE bare MCPs from the Cosmic Origins Spectrograph (COS–HST) have also been plotted. Some of the EUV MCP stacks were fairly close to nominal, but others were as much as a factor of two low. This is similar to problems that were encountered on the ALEXIS and FUSE missions. In both cases this has been investigated and seems to be due to a deficiency in the MCP detection efficiency for low energy electrons. This effectively means that the low energy photoelectrons emitted as the result of a photon interaction do not have a high probability for initiating a multiplication avalanche in the MCP. Recent work has indicated that this problem can be overcome by careful adjustment of the MCP processing steps. However this was too late to benefit the EUV program. Nevertheless, the bare MCP efficiency was used because the ratio of in-band

Figure 20. Background event image for EUV #04 detector, gain 7×10^6, 3650 V, 0.48 cnts s^{-1} cm^{-2}.

(30.4 nm) QDE to out-of-band QDE (>100 nm) is far larger than that available for any photocathode material.

3.4.2.3. *Background Rate.* The background characteristics of the curved surface MCP stacks were determined from PHD accumulations, and associated images of the background event positions taken over the same time period. The background event images also show a generally uniform spatial distribution of events (Figure 20). In some cases, however, there were some hot spots evident. The number of hot spots and the general background tended to decrease after burn-in and with increasing time under vacuum. The PHDs obtained were generally of the negative exponential curve shape that is characteristic of MCP stacks (Fraser et al., 1987). The pulse amplitude distribution for the curved MCP stack in detector #04 is shown in Figure 21. The curved MCP stacks had not been preconditioned prior to these measurements, and the range of background rates (0.3 to 0.8 events cm^{-1} s^{-2}) for the flight detectors is comparable to the rates observed for unconditioned flat MCP stacks with the same total L/D (Fraser et al., 1987; Siegmund et al., 1988). Thus the background due to β-decay from ^{40}K in the MCP glass (Fraser et al., 1987; Siegmund et al., 1988) and the adsorbed gasses in the MCP channel walls, are the major contributors.

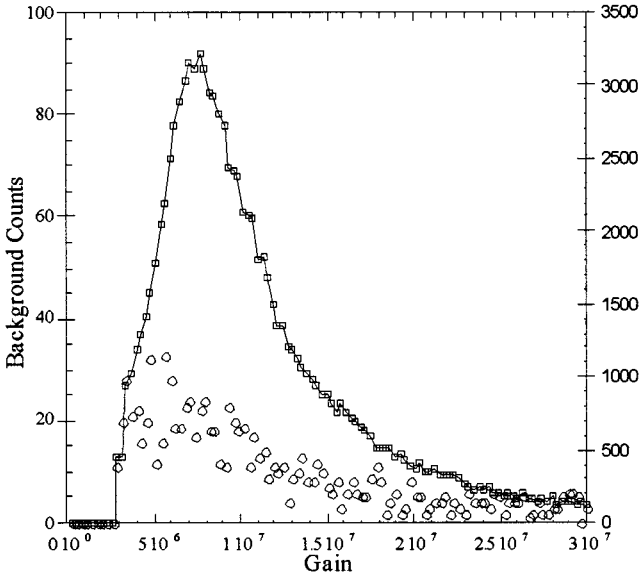

Figure 21. Background and signal event pulse amplitude distribution for the data in Figure 20.

3.4.2.4. *Preconditioning.* The flight MCPs were not subjected to extensive preconditioning on the basis that neither the in-orbit flux history nor the pre-launch handling requirements would permit effective preconditioning. However, the flight MCP stacks were subjected to a mild burn-in and bake. Bake was accomplished by raising the temperature to just over 100 °C for a period of about 8 hours, during which the pressure increased from the low 10^{-6} torr level to about 10^{-5} torr before decreasing again. The effect of the bake is largely to outgas water vapor from the MCPs and the detector structures. The gain curve and background after bake-out were not significantly different from those prior to bake-out.

During burn-in the MCP stacks were uniformly illuminated with UV radiation (253.7 nm) from an Hg lamp. The MCPs were operated at gains of about $2-5\times10^5$, with an output current of $\sim$0.1 μA cm^{-2}, which corresponds to an input intensity of about 2×10^6 photoelectrons cm^{-2} s^{-1}. As the MCP gain dropped during burn-in, the applied voltage was adjusted to maintain the output current. The burn-in was stopped after about 0.01 Coulombs cm^{-2} were extracted. The total gain drop observed was between a factor of 3 and 5, in accord with the range seen in earlier observations using flat MCP stacks (Siegmund, 1989). The gain vs. voltage curves for the #03 detector MCP stack before and after the burn-in are shown in Figure 22. After burn-in the gain at 3500 V had dropped by a factor of 3, but increasing the voltage restores the gain. This behavior agrees well with previous results for Z-stack MCPs with the same total L/D and obtained from the same manufacturer (Siegmund, 1989). The operating voltages established in testing after the burn-in are only about two-thirds of the full capacity of the high-voltage power supply, we have the flexibility to compensate for further gain loss in operation. We can

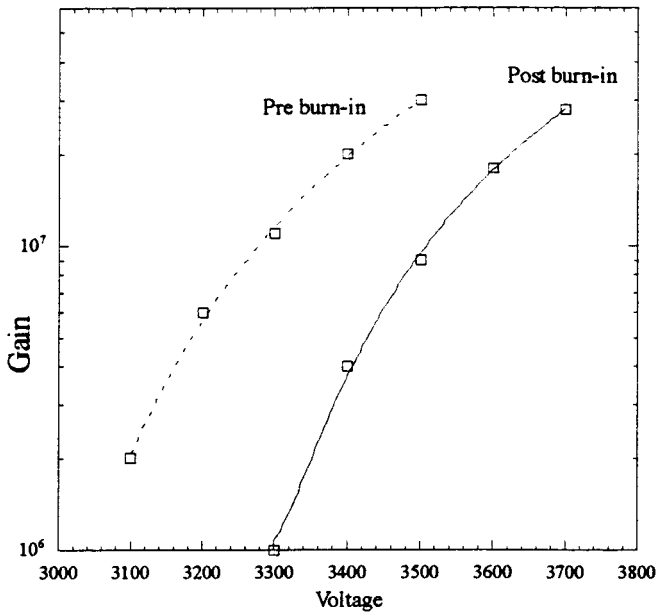

Figure 22. EUV #03 detector burn in gain vs. voltage curves.

assess changes in gain in flight by examining the pulse-height distribution of each detector.

3.4.2.5. *Image Linearity and Resolution Performance.* The image linearity and resolution of the detectors was measured by imaging an array of pinholes in a metal mask illuminated by a UV lamp. Since the surface of the MCPs is spherical it was not possible to place the flat mask directly in contact with the MCPs. Therefore, the mask was placed on the input face of the detector clamp to project the image pattern onto the spherical surface. This produces a predictable plano-to-spherical image mapping for our tests. Diffraction and parallax effects in the pinhole images become more pronounced in moving from center to edge, as the distance between the mask and MCP surface increases. Nevertheless, given the resolution requirements for the EUV instrument, these effects are relatively unimportant. Figure 23 is a representative pinhole mask image. This image shows the level of distortion of the image for the wedge and strip image readout. In the early stages of the program we employed wedge and strip substrates of fused silica that were spherically curved to match the MCP curvature. These gave image distortions that were similar to those of the ALEXIS detectors, and they were also subject to image stripes owing to differential non-linearity in the strip encoding axis. We found that a flat anode substrate gave better imaging performance. Image distortions in the spherical/spherical configuration arise mainly because the MCP charge clouds at the edge of the field overlap the edge of the anode pattern, which is virtually the same size as the encoded image area. The flat anode geometry both allows for a larger encoding

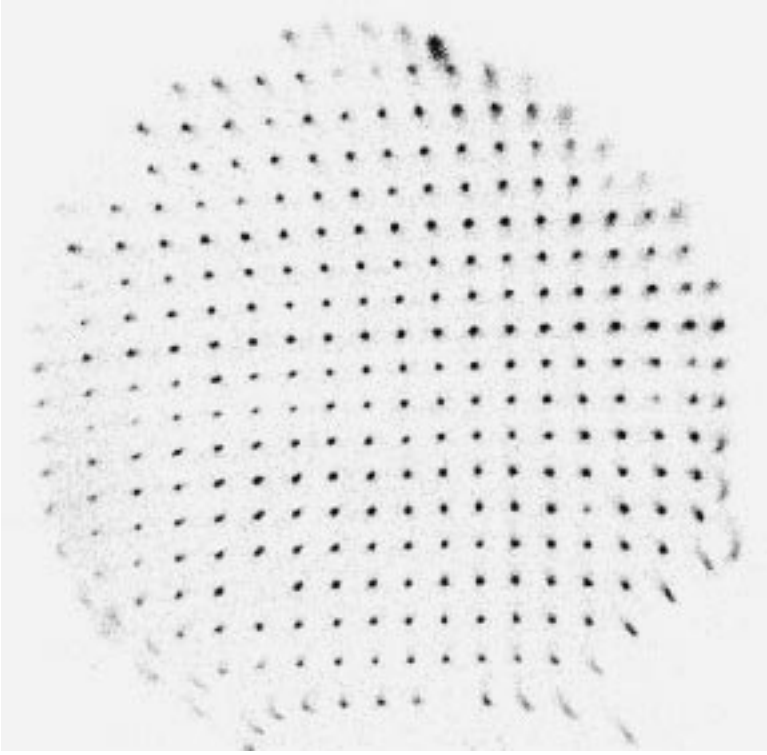

Figure 23. EUV #01 detector image of a mask having a square grid of 10 μm pinholes on 2 $\times$ 2-mm centers.

area and minimizes the charge cloud size at the image edges, resulting in the better performance. As shown in Figure 24, there is still significant distortion at the edge, which is mainly due to mis-encoding of the charge cloud centroids as a result of charge falling outside anode encoding area. Even so, the distortions are stable, so they can be characterized and corrected. The spatial resolution can be estimated by measuring the width of the pinhole images (Figure 24). Operating at typical gain levels, 1×10^7, the resolution is $\sim$ 160 μm FWHM, which substantially exceeds the requirements ($\sim$ 300 μm) for EUV. The resolution is also a function of gain (Figure 25), as expected for wedge and strip readout systems (Siegmund et al., 1986b), degrading to $\sim$ 300 μm at 3×10^6 gain.

3.4.2.6. *Flat Field Performance.* Flat field images having a large number of events ($> 10^6$) were taken with full field UV illumination with 253.7 nm radiation through a quartz diffuser. Providing a fully uniform illumination is difficult due to the spherical MCP configuration and varying pore bias angle. Flat field images binned to 256 $\times$ 256 show spatial variations in the detected images (Figure 26). These arise partly from variations in MCP detection efficiency and partly from defects in the MCP structure introduced in the curving process (note the central

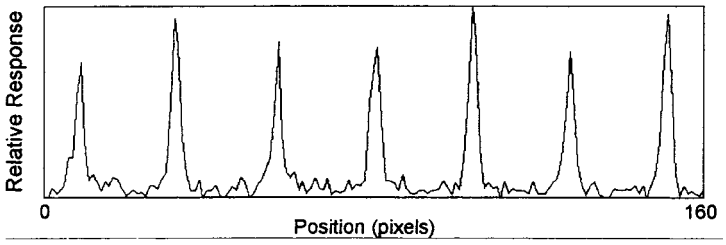

Figure 24. Pinhole image histogram, $\sim$ 165 μm FWHM resolution, 1.2×10^7 gain, EUV #04 detector.

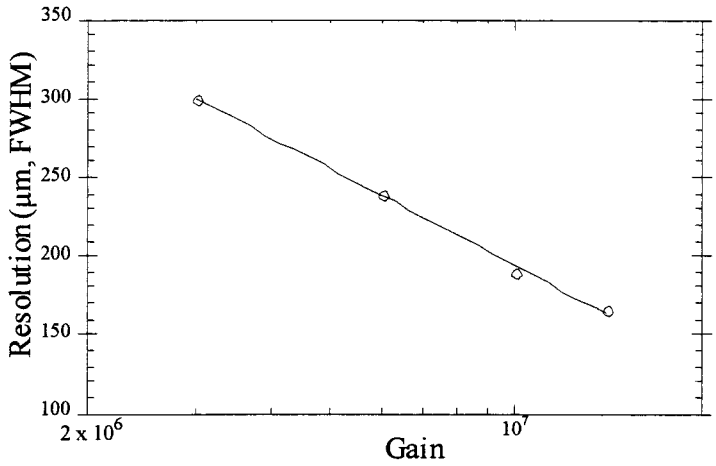

Figure 25. Mean resolution as a function of gain for the EUV #01 detector.

ring feature in Figure 26). The radial lines in Figure 26 are produced by the effect of the limited number of bits available for signal digitization, in particular for low amplitude events. However, the flat-field maps showed no features that correspond with the hexagonal multi-fiber boundaries of the MCPs. The area blocked by the MCP clamp ring is obvious as the missing area in the flat field image. Distortions on the flight detectors vary depending on the MCP stack gain uniformity and charge pulse width, as discussed in connection with image linearity. Gain maps, where the image intensity is replaced by the mean MCP gain for a given position, show the gain variations clearly (Figure 27). In all cases there is some gain variation from side to side, and in some cases (not chosen for flight) the gain varied in perfectly circular bands (bullseye pattern). These features are mainly attributable to the departures from spherical shape for the MCPs and mismatching of the spherical surface interfaces.

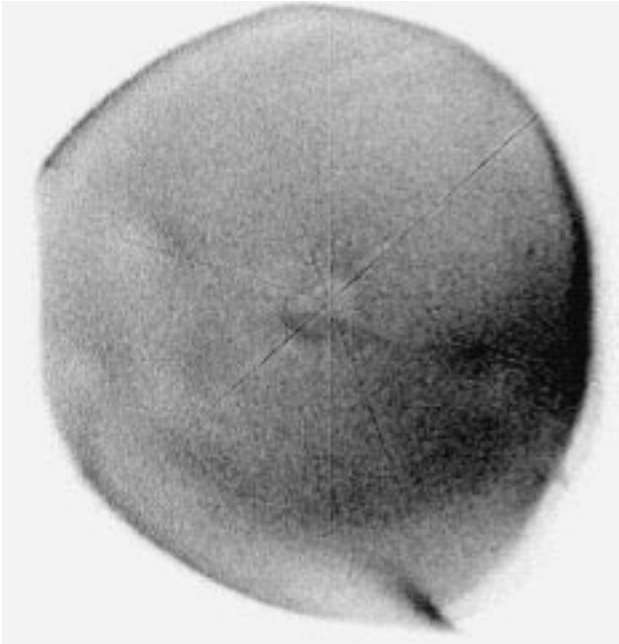

Figure 26. Flat field image for the EUV #02 flight detector. Uniform UV illumination, 4000 V applied.

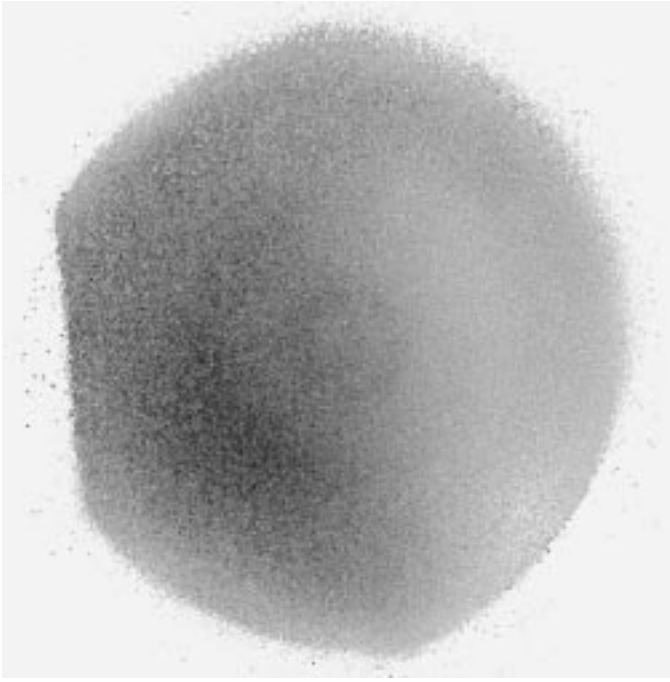

Figure 27. Gain map image for the EUV #04 flight detector, 3800 V applied.

4. Operation and Data Processing

As the IMAGE satellite spins, EUV integrates three maps (one for each sensor head) of 30.4 nm intensity. EUV's Controller keeps track of the satellite's spin phase by reference to two signals from CIDP, namely markers at intervals of 0.1° in spin phase (called here ticks) and a marker when Earth's center lies in the satellite's XZ plane (called here the nadir marker). With this information the Controller software can relate the position of each detected photon to a position in the sky. It then increments the value of the corresponding map array element. After a number of spins corresponding to the desired time resolution, the EUV transfers the sky map data to the CIDP, which compresses the image and formats it for the telemetry stream.

Determining the map array element that corresponds to the position of a detected photon involves several steps of computation. First, the wedge, strip, and zigzag signals from the detector are converted to an X,Y position on the detector using the equations given in Section 5.2. Using the tables described there, the X,Y position is transformed to an angular position in spacecraft coordinates. This transformation compensates for geometric distortions in the detector and for optical distortions inherent in the process of mapping the sky onto the spherical focal surface. Finally, the known roll phase is used to determine the appropriate array element in the skymap.

For each sensor head the skymap array consists of a 52×600 element array. The 600-element dimension of the array corresponds to roll phase. Each element represents an integration over 6 ticks, or 0.6° in roll phase. This increment was chosen to match the optical resolution of the sensor heads. Fifty elements of the 52-element dimension record spatial variations in the direction parallel to the spin axis. The remaining two elements for each roll phase record the number of dark counts and the number of out-of-range (error) events occurring at each increment of roll phase.

From time to time it may be useful to omit converting the W,S,Z data to X,Y values. For example, having access to the WSZ values permits certain diagnostic procedures that are not possible once the data have been processed to the skymap level. The WSZT data mode accommodates this need. By command, WSZT data can be substituted for the skymap data for any of the sensor heads. The former data consists of a list of the W, S, and Z values for each processed photoevent. Accompanying the triple of WSZ is a fourth parameter called T, which measures in units of 6 ticks the spin phase at which the event was recorded.

To help in interpreting the data in the skymap and WSZT array, the Controller computes arrays containing (1) the total event rate as a function of roll phase and (2) the MCP pulse height distributions. Each element in the event count array is a summation over 6 ticks (0.6° in roll phase) of counts on the Event Detected line from the detector electronics. This count therefore represents the rate at which events were recorded by the detector, rather than the rate at which events were

processed by the detector electronics to WSZ values. In case of count rates higher than can be fully processed to WSZ by the detector electronics, the information in the Event Count packet can help us to correct for the effects of pile-up. The pulse height distribution array represents the pulse height distribution of processed events, summed over one full EUV data cycle. This information can be helpful in evaluating detector performance and setting optimum gain levels.

At some times during the IMAGE Mission, the Sun will enter the field of one (and, rarely, two) of the sensor heads at certain spin phases. The aluminum filters will prevent damage to the detector by focused visible sunlight, but no useful data can be recorded from the affected sensor head with the Sun in the field. Therefore we will reduce the high voltage to the MCPs while the Sun is in the field to avoid excessive counting rates. EUV uses the Sun-position pulse from the CIDP to implement this. This pulse is transmitted to EUV once per roll at the time when the Sun lies in the spacecraft's XZ plane. By setting program control parameters, we can command EUV to reduce the MCP bias voltage to a safe level before the Sun enters the field and then return the bias to the operating level when the Sun has left the field. To avoid processing photoevents when the detector is not operating at full gain, the Controller inhibits event processing when the bias is reduced. Processing is resumed after a programmable delay interval that begins when the bias is restored to the operating level. The delay interval is chosen to be long enough so that the detector reaches full gain before photoevent processing is resumed.

The Controller is programmed for further autonomous protection in case the protection procedure described in the previous paragraph fails or an unanticipated bright source is detected. The Controller monitors the count rate from each sensor head continuously. If the rate exceeds a programmable threshold, the Controller reduces the MCP bias voltage to the affected sensor head. It then restores the voltage incrementally, at a programmable rate, until the normal operating level is reached.

Reporting data in the WSZT mode is much less efficient than using the skymap mode, and the telemetry array size limits the number of photoevents that can be accommodated to slightly fewer than 8000. When the array fills, no more events are processed until the array is read out and reset. Thus if there are two sources in the field at different roll phases, one source could fill the array and thereby prevent recording a signal from the second source. To avoid this problem, we have included a programmable processing window. This window operates independently of the solar protection algorithm. It permits us to limit processing of photoevents to those occurring in a specific range of roll phase angles.

Using the sensitivity found in Section 5.3, we can estimate count rates and the associated signal-to-noise ratio (SNR). The intrinsic dark count rate for an assembled sensor head is the sum of roughly equal contributions from (1) the intrinsic dark count rate of the detector (Section 3.4.2.3) and (2) the count rate stimulated by the radioactive component of the mirror coating. Our measurements show that the sum of these is $\sim$1 count cm^{-2} s^{-1}. For the measured sensitivity, the noise-

equivalent signal is then 0.03 R, where we have taken into account the duty cycle δ (Section 5.3) for operating on a spinning platform. For a 30.4-nm brightness of 0.1 R and the dark rate quoted above, we expect a SNR of 3 in each map element in a single 10 min integration. A brightness of 1 R yields SNR = 10 in the same integration time.

We must also consider the performance of the system for strong signals. The most challenging task is to accommodate the bright ionospheric emissions as Earth passes through the field of the center sensor head. For the wedge-and-strip readout, the important parameter is the count rate summed over the detector. If this count rate is too large, most of the processing time will be devoted to handling signals from Earth rather than the weaker (and desired) plasmaspheric emissions. Using a model of the ionospheric source, we estimate a worst-case instantaneous count rate of about 40 kHz summed over the detector. The count rate capability of the electronics (Appendix A) is 66 kHz, so it will be necessary to apply pile-up corrections under these worst-case conditions. The information in the Event Count packet is intended to help with this.

5. Calibration and Performance

5.1. Calibration system

Geometric and photometric calibration of the EUV were carried out in our EUV/FUV Calibration Facility at the Lunar and Planetary Laboratory. This calibration system includes a UV light source, a monochromator, and a test chamber with a gimbal support for the sensor head. The light source, monochromator, and test chamber are differentially pumped, because for EUV wavelengths no window materials can be used to separate them. EUV light for the calibration is produced by a DC glow discharge source, model LS101-DC, purchased from J.A.R. Samson's VUV Associates. The DC discharge excites a flowing gas to emit its characteristic spectrum, which in the EUV spectral range consists mainly of atomic lines. Light from the glow discharge source enters a modified Seya-Namioka monochromator, which selects the wavelength of interest from the input beam and collimates the exit beam in the horizontal plane. With the source focused to collimate the beam in the horizontal plane, the exit beam is slightly divergent in the vertical plane. For the conditions of our calibration setup, the divergence was about 0.04° full angle, a value that is small compared to EUV's spatial resolution of about 0.6° A grid collimator in the exit beam limits the spectral passband to about 1 nm. Stepper motors rotate the grating to select the wavelength and move the source to focus it so that the exit beam is collimated for all wavelengths.

As the beam from the monochromator enters the vacuum chamber, a portion of it strikes a channeltron beam monitor. This channeltron, called the continuous monitor, measures the beam intensity continually during an exposure in the EUV

instrument. Its signal is used to normalize the signals recorded by the EUV to a common input beam flux. This beam monitor is an important control on calibration quality, because the beam flux can change substantially over a few hours.

The gimbal in the vacuum chamber can rotate the instrument about two perpendicular axes (one horizontal and one vertical) and translate it in the plane defined by the two axes. The resolution is 787 steps cm^{-1} in translation and 60 steps deg^{-1} in rotation. The positions of the manipulator in its four degrees of freedom are maintained by the control computer. The positions are checked periodically by moving each axis to its maximum excursion, where it strikes a microswitch that serves as a position sensor. This microswitch also prevents mechanical damage to the manipulator that could result from overtravel. The repeatability of the switch positions was typically 2 to 3 steps, corresponding to a linear uncertainty of 0.003 to 0.004 cm and an angular uncertainty of 0.03° to 0.05°.

The calibration system was controlled by a single desktop computer running the Linux operating system. Interface cards in the same computer simulated the CIDP interface to EUV. This single computer controlled and monitored the calibration system, issued commands to EUV, and received and stored the resulting data from EUV. As a safety measure, a vacuum interlock signal provided by a cold-cathode vacuum gauge prevented operating the high voltage power supply when the tank pressure exceeded 5×10^{-6} torr.

For measurements of reflectivity and transmission, we used a second channeltron detector that could be positioned to measure either the input beam or the radiation reflected (or transmitted) by the material under test. With the intensity of the input beam measured relative to the continuous monitor, measuring reflectivity or transmission required only a relative measurement, so knowledge of the absolute response of this channeltron was unnecessary.

For absolute calibration of the throughput of the sensor heads, we relied on an EUV photodiode (Gullikson et al., 1996) that has been calibrated at NIST using the procedures described by Furst et al. (1995). The associated electronics produce a sinusoidal signal whose frequency is proportional to the intensity of the radiation striking the photodiode. Thus it was straightforward to substitute this diode for the reference channeltron and use the same counters to record and process the signal.

Because our calibration system produces a collimated beam of maximum diameter $\sim$1 cm, it was impossible to fill either the entrance aperture or the field of view of EUV. Instead, we have simulated the effect of filling the entrance aperture by making measurements with the beam at a number of positions within the aperture.

5.2. GEOMETRIC CALIBRATION

Calibration data were acquired by independently rastering EUV's three sensor heads in azimuth and elevation in the system gimbal. At each point in the raster a collimated pencil beam of He^+ 30.4 nm light was imaged in turn through the 4 quadrants of the entrance pupil mask (see Figure 2), and the data, in the form of raw

detector coordinates for single photoevents, were recorded to files in WSZT mode. The files of raw events were subsequently post-processed to convert the WSZ events into X,Y coordinates in the plane of the sensor using the transformations

$$q = W + S + 2Z \ , \tag{1}$$

$$X = k_x W/q - d_x \ , \tag{2}$$

$$Y = k_y S/q - d_y \ , \tag{3}$$

where W, S, and Z are the charge digitized on the wedge, strip, and zigzag electrodes. The parameters k_x and k_y are scale factors and d_x and d_y are shift factors that transform the normalized charge values to a cartesian detector coordinate system. We then extracted centroids, spot sizes, and relative intensities from the X, Y pairs associated with each (az,el). In these calculations, the data from each of the quadrants at fixed (az,el) were given equal weight, and the relative intensities were estimated by normalizing the total event count by the number of counts in the continuous monitor measuring the He^+ 30.4 nm source intensity. Collectively, these data form a geometry database whose keys are the manipulator (az,el) coordinates, and whose values are estimates of the image centroid, spot size, and relative sensor head efficiency at that point (see Figure 28). The (az,el) or X, Y entries not falling on the raster, which used a grid spacing of 2° in az and el, were obtained by extrapolation and/or interpolation. Dark frames were also acquired.

In the gimbal, the sensor heads were mounted on an elevation stage, which in turn was mounted on (and rotated with) an azimuth stage. At az = el = 0°, (a) the sensor boresight, elevation axis and azimuth axis formed a right hand triple; (b) the incoming He^+ 30.4-nm beam was anti-parallel to the sensor boresight; and (c) the detector wedge and strip axes were roughly aligned with the azimuth and elevation axes respectively (wedge changes most rapidly with elevation and strip most rapidly with azimuth). The directions of the He^+ 30.4-nm beam and the azimuth axis were fixed in the laboratory reference frame, and from the above discussion can be seen to be orthogonal. Knowledge of each sensor head's orientation in the gimbal was acquired from measurements on front and back alignment mirrors taken with a theodolite and by using a biaxial inclinometer, which was attached as necessary during each of several alignment steps which took the sensor heads from the gimbal to their integration and relative alignment into EUV's mechanical structure. The front and back alignment mirrors located each sensor head's optic axis, while the inclinometer determined a clocking angle about that axis.

5.2.1. *Construction of the Affine Tables*

On orbit, EUV's flight software creates a 52 × 600 pixel skymap in real time by using table lookup to implement a time-delayed-integration (TDI) algorithm. In essence, the algorithm takes raw WSZ events from a sensor head and computes an inertial coordinate pair in the skymap. Each sensor head has five tables. The first

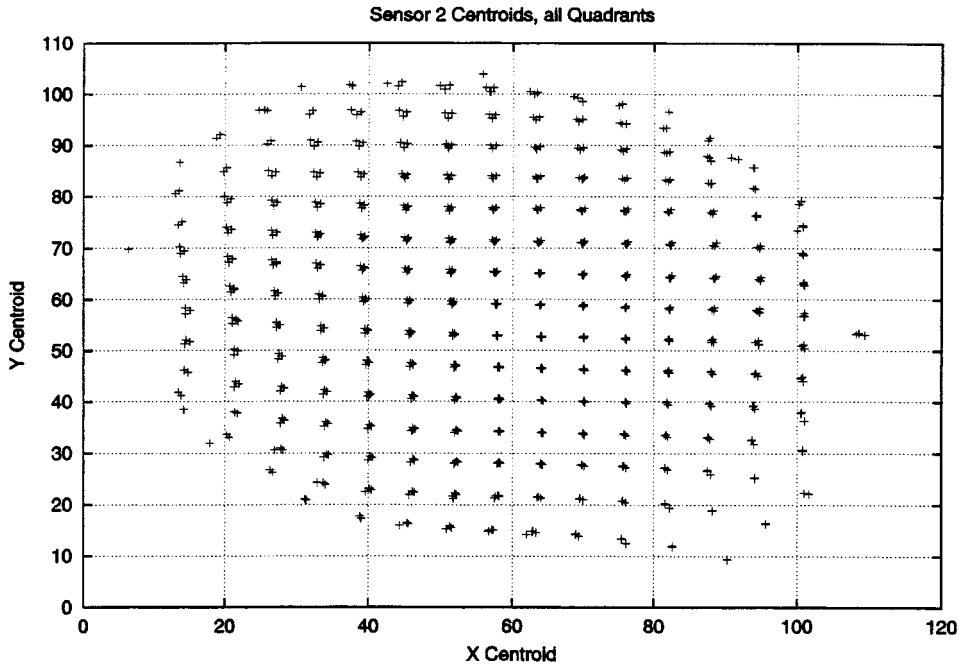

Figure 28. An example of the measurements of beam positions used in the geometric calibration.

four, Qx, Qy, Ax and Ay, are one-dimensional lookup tables which implement the transformation from WSZ to X, Y described above. The Qx and Qy tables, when indexed with the charge q in the event, return a number proportional to q^{-1}. This value multiplied by either S or W is used as an index into the Ax or Ay tables which implement the affine transformation equations. The constants of the transformation are determined from the calibration data by requiring that points in the FOV map to X, Y coordinates in the range 0 to 126 inclusive. The table entries have been chosen to minimize the R.M.S. error between the X, Y coordinates they produce and X, Y values calculated using floating point arithmetic. The ensemble for the calculation was generated from all possible WSZ events with charge $q \geq q_{\min}$, the smallest event charge consistent with proper detector operation (determined from the device physics and calibration data). Some events lead to values that are out of range (for example $q < q_{\min}$, $x < 0$, $y > 126$). Since comparisons are an expensive operation for the flight software, the tables were adjusted to map out-of-range events to coordinate 127. As a consequence, if X, Y pairs are used to construct a virtual 128×128 image of events, data in row 127 or column 127 will be out of range data. (We use the C-language convention that array indices range over the interval 0 to $N - 1$ inclusive for an array of length N.)

5.2.2. *Construction of the Distortion Tables*

Instantaneous virtual images formed by the coordinates X, Y will be in focus if the optics are in focus, but will suffer from distortions which preclude TDI operation. These include distortions intrinsic to the sensor, distortions in the optics, field curvature, rotations of the FOV about the camera optic axis, and geometrical or projective effects such as curvature and compression that are functions of the angle that the sensor head boresight makes to the spin axis of the satellite. These effects are removed by the fifth table associated with each sensor head. It is a 128×128 lookup table indexed by the X, Y coordinates resulting from the affine transformation. It returns a 'distortion free' coordinate pair in the range (52,50) that may be used to construct a TDI skymap. Constructing this table requires knowledge of each sensor head's orientation on the spacecraft.

When a sensor head is mounted on the spacecraft, alignment mirrors are used to determine the transformation between its local coordinates and a spacecraft system defined by the on-orbit spin axis and two other independent axes in the scan plane. Of particular importance are the angle that the sensor head boresight makes to the on-orbit spin vector and the clocking angle about the boresight. These are similar to the parameters that were used to fix the attitude of a sensor head in the gimbal and then integrate it into EUV. The remaining degree of freedom, a spin phase angle, is less important since errors in its knowledge can be removed during ground-based processing.

Construction of the distortion correction table is now straightforward. Time-Delayed Integration (TDI) operation requires that one sensor head coordinate depend only on the elevation of a point source above or below the scan plane of the spacecraft, while the other must vary linearly with the spin phase. Alignment knowledge acquired during calibration and spacecraft integration allow one to calculate the required TDI coordinates of any point source in the sky. The cells of the table are then chosen to map distorted points measured during calibration into a pair of corrected indices suitable for TDI. The corrected indices fall within a 50×50 pixel virtual image of the FOV and the TDI transformation is applied in real time, using the time component of the WSZ event, onto rows $0-49$ of the 52×600 pixel skymap.

Two further complications must be dealt with. Out-of-range data have one or more coordinates with the special value 127. These cells in the distortion correction table are assigned the values (50,0) so that all out-of-range data eventually finds its way to row 50 of the skymap. The second complication is related to the detector dark count rate. Part of the active area of each detector is masked to provide a dark event region. The coordinates of the events from this area can be determined from the calibration data, and the corresponding cells in the distortion table set to (51,0), so that row 51 of the skymap is a measure of the dark current.

5.2.3. *Flat Fields and Resolution*

As the spacecraft spins, the image of each point in the sky follows a trajectory over the detector that is subsequently collapsed to a single point in the skymap by a TDI operation. To generate a flat field for a TDI skymap, one must first calculate, using the calibration alignment data, the trajectory that each point in the skymap must have followed, and then average the effective detector QDE measured during the calibration raster scans over this path. Similar statements can be made about the sensor resolution.

5.3. PHOTOMETRIC CALIBRATION

For a uniformly-bright source of intensity 1 R that fills a resolution element, and for field points near the optic axis (where vignetting can be neglected), the counting rate is

$$S = A\omega\epsilon\tau\rho\frac{10^6}{4\pi}\ , \tag{4}$$

where A = open aperture = 21.8 cm^2, ω = solid angle of spatial resolution element = 1.1×10^{-4} sr, ϵ = quantum efficiency of the detector = 0.14, τ = filter transmission = 0.33, and ρ = reflectivity of mirror = 0.22.

Using the values for the parameters given above, we find $S = 1.9$ count s^{-1} R^{-1}. The product $S\delta$, where δ is the duty cycle for operating on a spinning platform ($\delta = 30°/360° = 0.083$) is the parameter to use to estimate the on-orbit performance of EUV in terms of signal rate and signal-to-noise ratio. However, for comparison with laboratory calibration work using a collimated beam, the appropriate parameter for comparison is the photon conversion efficiency,

$$E = \epsilon\tau\rho\ , \tag{5}$$

for which, using the values of the parameters given above, we find $E = 1.02 \times 10^{-2}$ counts photon^{-1}. For the flight sensor heads we have determined this efficiency using the same laboratory calibration data used for the geometric calibration. In all cases we find values that are consistent with the individual values of the three parameters.

5.4. IN-FLIGHT CALIBRATION

In-flight calibration will be useful (1) to assess the throughput of EUV and thereby account for possible aging or contamination effects, and (2) to verify that the TDI operation is working correctly, and hence that our understanding of the position of the spin axis in an EUV coordinate system is correct. Nearby sources suitable for in-flight calibration of EUV include Earth and the Moon. Because of its large size and uncertain brightness at 30.4 nm, Earth is not particularly useful for either geometric or photometric calibration. On the other hand, the Moon (diameter 0.5°)

is comparable in size to our resolution element (0.6°) and has been fairly well characterized by the Extreme Ultraviolet Explorer (EUVE) (Gladstone et al., 1994). Using EUVE measurements, we estimate an instantaneous count rate of 230 Hz (or 10^4 counts in 10 min) from the Moon under conditions of favorable observing geometry. One early test will be to verify our transformation tables by observing the Moon in both skymap and WSZT modes. This observation will be planned for a time near full Moon when the IMAGE orbit is near the noon-midnight meridian. The Moon's orbital motion will carry it slowly through the field of all three sensor heads.

Interstellar hydrogen absorbs strongly at 30.4 nm, so most astrophysical sources are not useful calibration targets in the EUV. However, in some directions the interstellar H column density is unusually low, and certain sources in these directions can be detected in the EUV. The brightest such source is the white dwarf HZ-43, which has a continuum flux of about 1.36 photons cm^{-2} s^{-1} nm^{-1} near 30.4 nm (Barstow et al., 1995). Although the spectral distribution is a continuum, the passband established by the mirror reflectivity is narrow enough to limit the response of EUV to wavelengths near 30.4 nm, for which the sensitivity of the sensor heads is well known. For the measured mirror passband of 4.0 nm we anticipate a signal of 60 counts in a 10-min exposure. This will be sufficient for a reliable measurement given the integration times available in orbit.

6. Data Products and Analysis

6.1. The structure of EUV telemetry packets

EUV transmits data that have been organized into telemetry packets according to their type. Table III summarizes the characteristics of each of the packets. The notation 0, 1, 2 in the name of some of the packets indicates that separate packets are produced for each of the three sensors heads, which we number 0, 1, and 2.

In its nominal observing mode, the EUV returns science data in the Skymap, Event Count, and Pulse Height Distribution (PHD) packets. The Skymap data packet contains the fundamental measurements of sky brightness seen by each of the sensor heads (Section 4). The WSZT packet records up to the maximum number of events shown in Table III in the raw data mode called WSZT (Section 4).

Engineering data appear in the Status and Diagnostic Housekeeping (DHK) packets. The Status packet reports the values of all the software registers that control and reflect the functioning of EUV, as well as the 16 analog voltage, current, and temperature monitors. It also includes a command history. The DHK packet contains the values of the 16 analog monitors sampled at the rate of 2 Hz. This information is of most interest in connection with tracking the performance of the HVPS when EUV enters a sun-protection or over-rate protection mode. For diagnostic and verification purposes, we can command EUV to dump a specified part of its RAM space. These data appear in the Memory Dump packet.

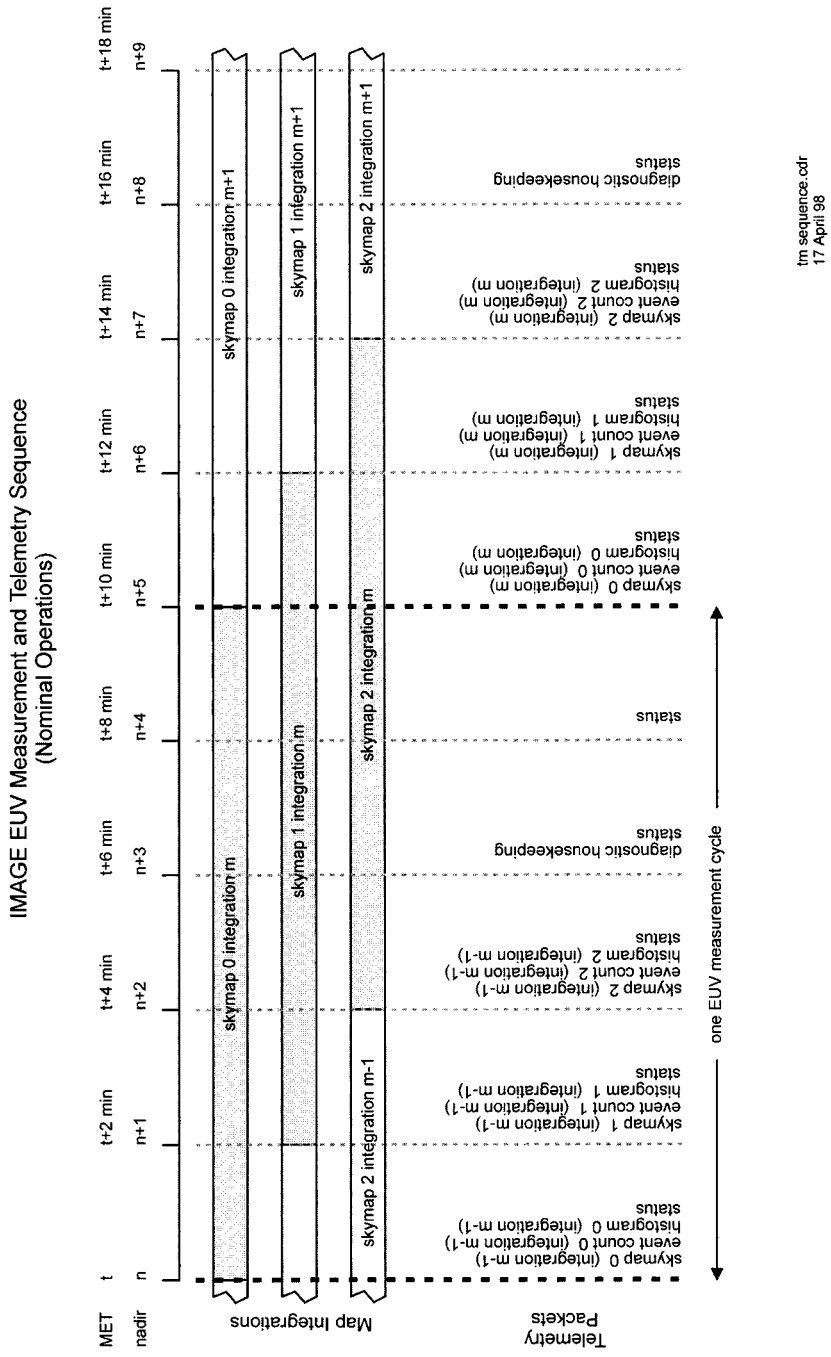

Figure 29. The EUV telemetry cycle, showing the offset in integration times for the three skymaps.

TABLE III
EUV telemetry packets

Packet Name	Size (bytes)	Function
Skymap 0, 1, 2	62440	600×52-element array of 30.4 nm brightness
Event count 0, 1, 2	7240	600-element array of count rates
Pulse height distribution	2088	1024-element pulse height distribution
WSZT 0, 1, 2	62440	4×7798 (max) array of raw event coordinates
Status	2088	Engineering measurements and control program variables
Diagnostic housekeeping	38444	Voltages, currents and temperatures sampled at 2 Hz
Memory dump	variable	RAM contents

6.2. THE EUV TELEMETRY DATA CYCLE

In its nominal operating mode, EUV integrates skymaps over five spins of the satellite. To distribute the generation of telemetry packets conveniently over this time interval, we have adopted the scheduling shown in Figure 29. During the first three spins of each five-spin cycle, EUV transmits a Skymap packet, the associated Event Count and Pulse Height Distribution packets, and a Status packet. In the fourth spin EUV transmits DHK and Status packets, and in the final spin a Status packet alone. Because the skymap data are not double-buffered within EUV, the integration times for the three sensor heads are staggered relative to one another as shown in Figure 29. When WSZT mode is commanded for one or more sensor heads, the WSZT packet is simply substituted for the Skymap packet corresponding to that sensor head.

6.3. LEVEL 1 DATA

Processing Level 0 data (described above) to Level 1 data gives a product that is suitable for scientific analysis. The process begins with the individual Skymap data packets. The out-of-range count is examined to determine whether remedial processing or action is required. Then using the information in the Pulse Height Distribution packets, any needed corrections for detector counting efficiency are applied. Using information in the dark count sub-array from the Skymap packet, a dark count frame is subtracted from the map array. If needed, a correction for pile-up is applied, based on information in the Event Count packet. The last step in handling the skymap arrays individually is a flat-field correction based on laboratory calibration data and subsequent analysis.

The individual skymap arrays having now been fully processed, map arrays from the three sensor heads can be merged into a single map array, using information about the overlap of the fields of view of the three sensor heads from the laboratory geometric calibration. With this information, the distortion correction tables can be adjusted so that the positions of corresponding resolution elements in adjacent heads are properly registered. Therefore merging the maps does not degrade the spatial resolution. The merged map can then be converted to intensity units (R) using the laboratory photometric calibration. Finally, a standard Earth-fixed coordinate system is applied to the map array using orbit and attitude information from the spacecraft.

In accord with the policy established for the IMAGE Project, all IMAGE EUV data will be available to the scientific community without the limitation of a proprietary period. The NSSDC will provide Web-based access to 'browse products' that include a subset of the data from each instrument. The presentation will facilitate a quick overview of observations by a particular instrument and comparisons between related instruments. Also available from this source will be the Level 1 data and certain analysis software developed by the EUV team.

Appendix A. The EUV Electronics

A.1. Controller

The EUV Controller handles data processing, storage, and control functions for the EUV. Its main task is to accept the data from the three sensor heads in real time, process them, and store them for subsequent transmission to the CIDP. The Controller also commands the three output channels of the HVPS separately, communicates with the CIDP to transfer data and to synchronize data processing with the spin phase, and monitors voltages and temperatures.

Figure 30 is a functional block diagram of the EUV Controller, and Figure 31 is a block diagram of the circuitry. The heart of the controller is a Harris RTX2010 microprocessor. The block of 128 kbytes of RAM provides storage for the executing copy of the flight software and buffers for the maps and ancillary sensor data. The lookup tables needed to correct distortions and form the maps are stored in EEPROM, along with at least one copy of the flight code and selected operating parameters. The PROM holds the bootstrap code that operates the instrument at turn-on. To achieve the required throughput, much of the low-level processing of data from the sensor heads is performed in hardware, namely the two Actel RH1280 FPGAs. The FPGAs accept the data from the sensor heads, keep track of the spin phase, control the HVPS, provide UARTs for communications with the CIDP, and implement the watchdog timer functions. Where possible, the software is written in C, but the need for speed led us to use assembly language routines for about 15% of the code.

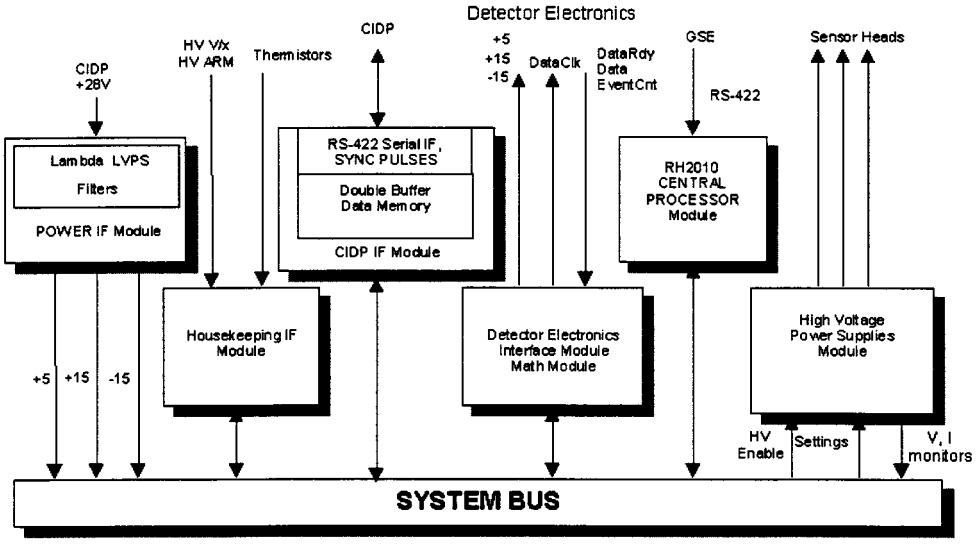

Figure 30. EUV controller functional block diagram.

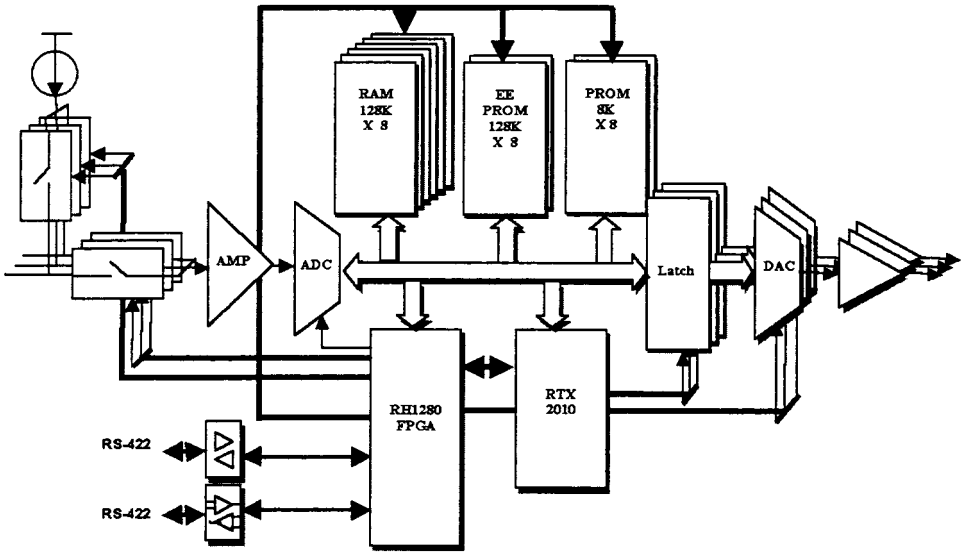

Figure 31. EUV controller electronics block diagram.

The event data from each sensor head have a maximum burst rate of 66 kHz and the maximum expected sustained rate is 10 kHz. Since the events are asynchronous, all three heads may present data to the Controller at the same time. To avoid losing data, the data from any head must be read into the memory queue within 5 μs. The Controller processes each event within 20 μs to assure that no data are lost in the queue. This leaves about 25% of the Controller's capacity free for housekeeping tasks and servicing the CIDP interface. The Controller commu-

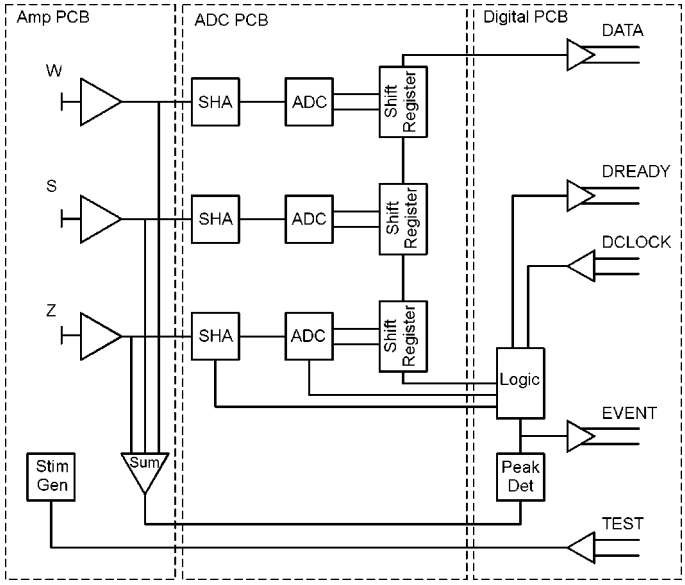

Figure 32. EUV detector electronics block diagram.

nicates with the CIDP via an RS-422 link at 38,400 baud. At each nadir pulse, the Controller transmits data packets to the CIDP according to the schedule described in Section 6.2.

Because the EUV must operate for long periods without ground contact, we have implemented three types of watchdog timers that will protect the instrument in case of an anomaly. The first of these, implemented in hardware, guards against a stuck microprocessor. This timer monitors processor activity. If it detects no activity for 3.4 s, it will reset the microprocessor, disable the HVPS, and set a status bit that can be read on start-up. The second watchdog timer monitors the regular 0.1° sync pulses from the CIDP. If these are missing for a period of 3.4 s, the software will command EUV to the SAFE state and set a status bit to record the origin of the safing. EUV will begin taking data again at the beginning of the next spin if the sync pulses are present. The third safety timer monitors the 'All-Is-Well' messages sent by the CIDP once per second. If these messages are not found for a period of 5 min, the software will put EUV in its SAFE state and set the appropriate status bit to record the reason for safing.

We have adopted a radiation design philosophy that includes parts with minimum radiation capability of 100 kRads. All parts are shielded with a minimum wall thickness of 0.38 cm of aluminum, which reduces the expected radiation dose over the course of the IMAGE mission to 50 kRads. Thus the radiation margin is a factor of approximately 2.0.

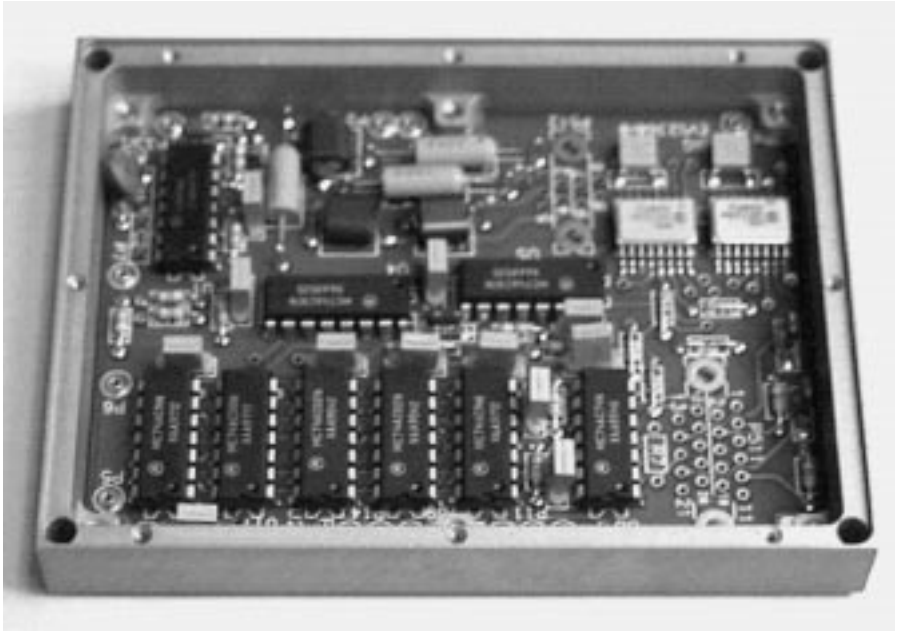

Figure 33. EUV interface electronics board and enclosure. Amplifier and ADC boards have the same footprint and stack below the I/F board.

A.2. DETECTOR ELECTRONICS

The EUV detector electronics for each sensor head (Figure 32) consist of three charge-sensitive amplifier channels (for the wedge, strip, and zigzag charge signals), three analog/digital conversion channels, and logic for generating the necessary timing signals for data transfer. The design is optimized for low power dissipation and adequate radiation hardness.

The charge sensitive preamplifier uses a large area junction FET for low noise, and unipolar shaping to minimize power. A simple stimulation pulse generator is included to produce simulated events that appear as two spots on the image for liveness and stability testing. A sample-hold circuit holds the peak values of the three circuits for conversion by the analog digital converter (ADC). The three ADCs are 12-bit radiation-shielded parts whose outputs are serialized by a set of shift registers.

The logic circuitry includes a window comparator to test that the total charge is within set limits, and circuitry to generate the necessary HOLD, READ, and CLOCK signals to control the ADCs. Total system power dissipation is less than 800 mW using $+15$, -15, and $+5$ V supplies.

The system is packaged as a set of three printed circuit boards (AMP, ADC, DIGITAL) which stack together in a series of frames (Figure 33). SMC connections are used for the signal inputs and the sum signal output monitor. Interboard

connections are made via single pin sockets. Connection to the EUV controller is via Micro D15 connectors for the data, and Micro D9 connectors for power.

A.3. High voltage power supply

The EUV High Voltage Power Supply is housed in a separate enclosure of size $21.6 \times 18.7 \times 4.1$ cm and mass 1.65 kg. It is mounted vertically on the left-side EUV support bracket, opposite the Controller electronics enclosure.

The HVPS is controlled by an enable line and three independent 12-bit D/A lines. The enable controls all three HV outputs. With the HVPS enabled, the output voltages for the three channels are independently selectable by the analog control lines in the range -200 to -6000 V. For an additional measure of safety for ground testing, an independent control line can be activated to confine the HVPS output voltage to the range -200 to -300 V, while permitting the oscillators and other circuits of the HVPS to operate. A second control line can be activated to disable the HVPS completely. The HVPS provides analog monitors of the output voltage and current to each of the three sensor heads.

To avoid high count rates when the Sun is in the field of view of a sensor head, the high voltage to that head is reduced before the Sun enters the field and restored to the operating level after the Sun leaves the field. The output of the HVPS changes with a time constant of $\sim$1.35 s. This means that the transition from low level selected for sun protection to an effectively stable operating level requires $\sim$6 s, an acceptably small fraction of the nominal 120-s spin period.

Acknowledgements

This work was supported by contract 83818 from Southwest Research Institute, a subcontract under contracts GSFC-410-MIDEX-001 and GSFC-410-MIDEX-002 from Goddard Space Flight Center. We thank Martin Valente of the University of Arizona's Optical Sciences Center, who supervised the grinding and polishing of the mirrors; Darrell Judge and Don McMullin of the USC Space Sciences Center, who supplied the photodiode used for absolute calibration; and Eric M. Gullikson, LBNL, who measured the mirror reflectivity vs. wavelength. Adam Fennimore and Carlos Vazquez-Lopez of Depto. de Fisica, CINVESTA, performed AFM and TEM measurements, and Ben Chao of Energy Conversion Devices, Inc. made AES measurements on multilayer mirror samples. The high voltage power supply was designed and tested by Steven Battel of Battel Engineering, and built at the Space Physics Research Laboratory of the University of Michigan. The major mechanical components were fabricated at the University of Arizona's University Research Instrumentation Center under the direction of James Izlar. The microchannel plates were provided by Photonis, and the filters were provided by Luxel Corporation.

References

Barstow, M. A., Holberg, J. B. and Koester, D.,: 1995, *Monthly Notices Roy. Astron. Soc.* **274**, L31.

Barstow, M. A. and Sansom, A. E.: 1990, *SPIE* **1344** 244.

Barstow, M. A., Fraser, G. W. and Milward S. R.: 1985, *SPIE* **597**, 352.

Bloch, J. J., Ameduri, F., Priedhorsky, G. W., Roussel-Dupre, D., Smith, B. W., Siegmund, O. H. W., Cully, S., Warren, J. and Gaines, G. A.: 1990, *SPIE* **1344**, 154.

Carpenter, D. L., Giles, B. L., Chappell, C. R., Decreau, P. M. E., Anderson, R. R., Persoon, A. M., Smith, A. J., Corcuff, Y. and Canu, P.: 1993, *J. Geophys. Res.* **98**, 19,243–19,271.

Carpenter, D. L.: 1995, *EOS, Trans. Am. Geophys. Union* **76**(9), 89–92.

Chakrabarti, S., Paresce, F., Bowyer, S., Chiu, S. and Aikin, A.: 1982, *Geophys. Res. Lett.* **9**, 151.

Fennimore, A., Allred, D., Turley, R. S., Vazquez, C. and Chao, B.: 1999, *Appl. Optics* (submitted).

Furst, M. L., Graves, R. M., Canfield, L. R. and Vest, R. E.: 1995, *Rev. Sci. Instrum.* **66**, 2257.

Fok, M.-C., Moore, T. E., Kozyra, J. U., Ho, G. C. and Hamilton, D. C.: 1995, *J. Geophys. Res.* **100**, 9619–9632.

Fraser, G. W., Pearson, G. F. and Lees, J. E.: 1987, *Nucl. Instrum. Meth.* **A254**, 447.

Fraser, G. W.: 1984, *Nucl. Instrum. Meth.* **221**, 115.

Gladstone, G. R., McDonald, J. S., Boyd, W. T. and Bowyer, S.: 1994, *Geophys. Res. Lett.* **21**, 461.

Gullikson, E. M., Korde, R., Canfield, L. R. and Vest, R. E.: 1996, *J. Electron Spect. Rel. Phen.* **80**, 313.

Khazanov, G. V. and Liemohn, M. W.: 1995, *J. Geophys. Res.* **100**, 9669–9681.

Lunt, S.: 1999, The Use of Genetic Algorithms in Multilayer Mirror Optimization, BYU Honors Thesis.

Lunt, S. and Turley, R. S.: 1998, *Physics of X-Ray Multilayer Structures* **4**.

Lunt, S. and Turley, R. S.: 1999a, *Proc. Utah Acad.* (submitted).

Lunt, S. and Turley, R. S.: 1999b, *J. X-Ray Sci. and Tech.* (submitted).

Meier, R. R. and Weller, C. S.: 1974, *J. Geophys. Res.* **79** 1575.

Meier, R. R., Nicholas, A. C., Picone, J. M., Melendez-Alvira, D. J., Ganguli, G. I., Reynolds, M. A. and Roelof, E. C.: 1998, *J. Geophys. Res.* **103**, 17505.

Priedhorsky, G. W., Bloch, J. J., Smith, B. W., Strobel, K., Ulibarri, M., Chavez, J., Evans, E., Siegmund, O. H. W., Marshall, H., Vallerga, J. and Vedder, P.: 1988, *SPIE* **982**, 188.

Sandel, B. R., Drake, V. A., Broadfoot, A. L., Hsieh, K. C. and Curtis, C. C.: 1993, *Remote Sensing Rev.* **8**, 147.

Siegmund, O. H. W.: 1989, *SPIE* **1072**, 111.

Siegmund, O. H. W.: 1988, *SPIE* **982**, 108.

Siegmund, O. H. W., Vallerga, J. and Lampton, M.: 1988, *IEEE Trans. Nucl. Sci.* **NS-35**, 524.

Siegmund, O. H. W., Vallerga J., and Jelinsky, P.: 1986a, *SPIE* **689**, 40.

Siegmund, O. H. W., Lampton, M., Bixler , J., Chakrabarti, S., Vallerga, J., Bowyer, S. and Malina, R. F.: 1986b, *J. Opt. Soc. Am.* **A3**, 2139.

Siegmund, O. H. W., Coburn, K. and Malina, R. F.: 1985 *IEEE Trans. Nucl Sci.* **NS-32**, 443.

Skulina, K. M.: 1995, *Appl. Optics* **34**, 3727.

Squires, M. B.: 1999, On Determining the Optical Constants of Sputtered U and a-Si at 304 and 584 Å, BYU Honors Thesis.

Thomsen, M. F., McComas, D. J., Borovsky, J. E. and Elphic, R. C.: 1998, *AGU Monograph: Geospace Mass and Energy Flow* **104**, 355–369.

Vallerga, J. V., Vedder, P.W. and Siegmund, O.H.W.: 1992, *SPIE* **1742**, 392.

Williams, D. J.: 1990, in B. Hultqvist and C. G. Falthammer (eds.), *Magnetospheric Physics*, Plenum Press, New York, pp. 83–101.